

Enhancing Anticancer Cytotoxicity through Bimodal Drug Delivery from Ultrasmall Zr MOF Nanoparticles

Isabel Abánades Lázaro,^a Sandra Abánades Lázaro,^a Ross S. Forgan^{a*}

^a*WestCHEM, School of Chemistry, University of Glasgow, University Avenue,
Glasgow, G12 8QQ, UK.*

E-mail: Ross.Forgan@glasgow.ac.uk

SUPPORTING INFORMATION

TABLE OF CONTENTS

S1.	General Experimental Remarks	S2.
S2.	Synthesis and Characterisation of Zr-LX_{small}	S4.
S3.	Synthesis of DCA@MOFs of Larger Size	S15.
S4.	Colloidal Stability of DCA@MOFs	S22.
S5.	Therapeutic Efficiency of DCA@MOFs	S26.
S6.	5-FU Loading	S30.
S7.	Therapeutic Efficiency of 5-FU@DCA@MOFs	S35.
S8.	References	S39.

S1. General Experimental Remarks

Powder X-Ray Diffraction (PXRD): PXRD measurements were carried out at 298 K using a PANalytical X'Pert PRO diffractometer (λ (CuK α) = 1.4505 Å) on a mounted bracket sample stage. Data were collected over the range 5–45 °. (University of Glasgow)

Thermogravimetric Analysis (TGA): Measurements were carried out using a TA Instruments Q500 Thermogravimetric Analyser. Measurements were collected from room temperature to 800 °C with a heating rate of 10 °C / min under an air atmosphere. (University of Glasgow)

Nuclear Magnetic Resonance Spectroscopy (NMR): NMR spectra were recorded on either a Bruker AVIII 400 MHz spectrometer or a Bruker AVI 500 MHz spectrometer and referenced to residual solvent peaks. (University of Glasgow)

Gas Uptake: N₂ adsorption isotherms were carried out at 77 K on a Quantachrome Autosorb iQ gas sorption analyser. Samples were degassed under vacuum at 120 °C for 20 hours using the internal turbo pump. BET surface areas were calculated from the isotherms using the Micropore BET Assistant in the Quantachrome ASiQwin operating software. (University of Glasgow)

Pore-Size Distribution: Pore size distributions were calculated using the N₂ at 77 K on carbon (slit pore, QSDFT, equilibrium model) calculation model within the Quantachrome ASiQwin operating software. (University of Glasgow)

UV-Vis Spectroscopy: UV-vis spectra were recorded using a Shimadzu UV-1800; analysis was carried out using the software UVProve. (University of Glasgow)

Scanning Electron Microscopy (SEM): The powder samples were coated with Pd for 150 seconds using Polaron SC7640 sputter coater and imaged using a Carl Zeiss Sigma Variable Pressure Analytical SEM with Oxford Microanalysis. Particle size distribution was analysed manually using ImageJ software. (University of Glasgow)

Infrared Spectroscopy: Infra-red spectra of solids were collected using a Shimadzu Fourier Transform Infrared Spectrometer, FTIR-8400S, fitted with a Diamond ATR unit. (University of Glasgow)

Dynamic Light Scattering: Colloidal analysis was performed by Dynamic Light Scattering (DLS) with a Zetasizer Nano ZS potential analyser equipped with Non-Invasive Backscatter optics (NIBS) and a 50 mW laser at 633 nm. (University of Glasgow)

S2 Synthesis and Characterisation of Zr-LX_{small}

Attempts to prepare small (sub 50 nm) particles of the MOFs Zr-L1 to Zr-L6 followed the general procedure below:

In separate vessels, zirconyl chloride octahydrate (213 mg, 0.66 mmol, 1 equivalent) and the linker (1.65 mmol, 2.5 equivalents) were dissolved in 25 mL of DMF. After mixing both precursor solutions in a 80 mL vial, dichloroacetic acid (DCA, 1 mL, 12 mmol, 18.2 equivalents) was added to the reaction mixture which, after gently stirring, was placed in the oven at 120 °C for 24 h. After cooling to room temperature, the powders were collected by centrifugation, and washed with DMF (X2) and MeOH (X3) through dispersion centrifugation cycles. The resultant NMOFs were dried under vacuum for at least 24 hours prior to analysis.

Powder X-ray diffraction (PXRD) patterns (Figure 2a, main text) show Bragg reflection peaks characteristic of the UiO-66 topology. In the case of the UiO-66 derivatives, wide peaks with low intensity and poor definition are observed, suggesting small nanoparticles with defected structures. Structures containing L5 and L6 as linkers are more crystalline and the reflection peaks are considerably narrower, thus indicating bigger and less defective nanoparticles. In contrast to recently reported UiO-66 gels^{S1} and other reported defective UiO-66 type structures,^{S2} no extra reflection peaks (usually attributed to the defective **reo** topology, in which missing clusters give locally eight-connected nets^{S3}) were found in the PXRD patterns.

SEM imaging was used to study the morphology and size of the NMOFs, showing that while the DCA@Zr-LX_{small} derivatives of linkers L1-L4 are indeed small nanoparticles (Figures S1 and S2) of slightly different sizes (10-30 nm, particle size distribution in Figure S3) depending on the linker, DCA@Zr-L5 and DCA@Zr-L6 are composed of bigger nanoparticles (Figure S4, particle size distribution in Figure S5). The average particle sizes and standard deviations are shown in Table S1).

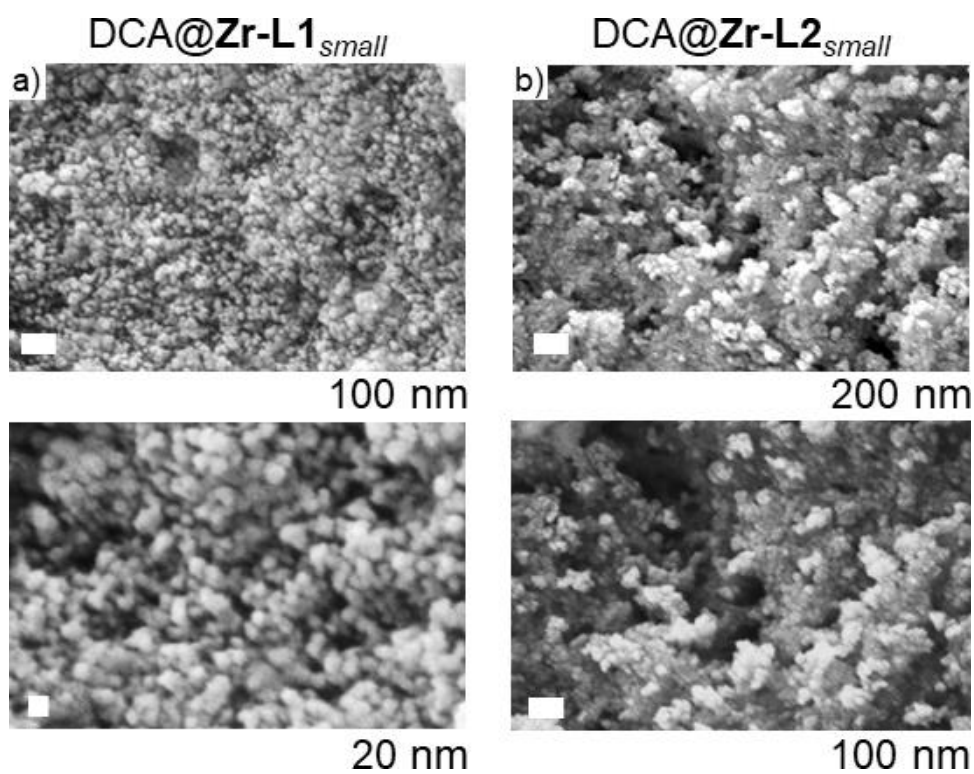


Figure S1. SEM images of a) DCA@Zr-L1_{small} and b) DCA@Zr-L2_{small}.

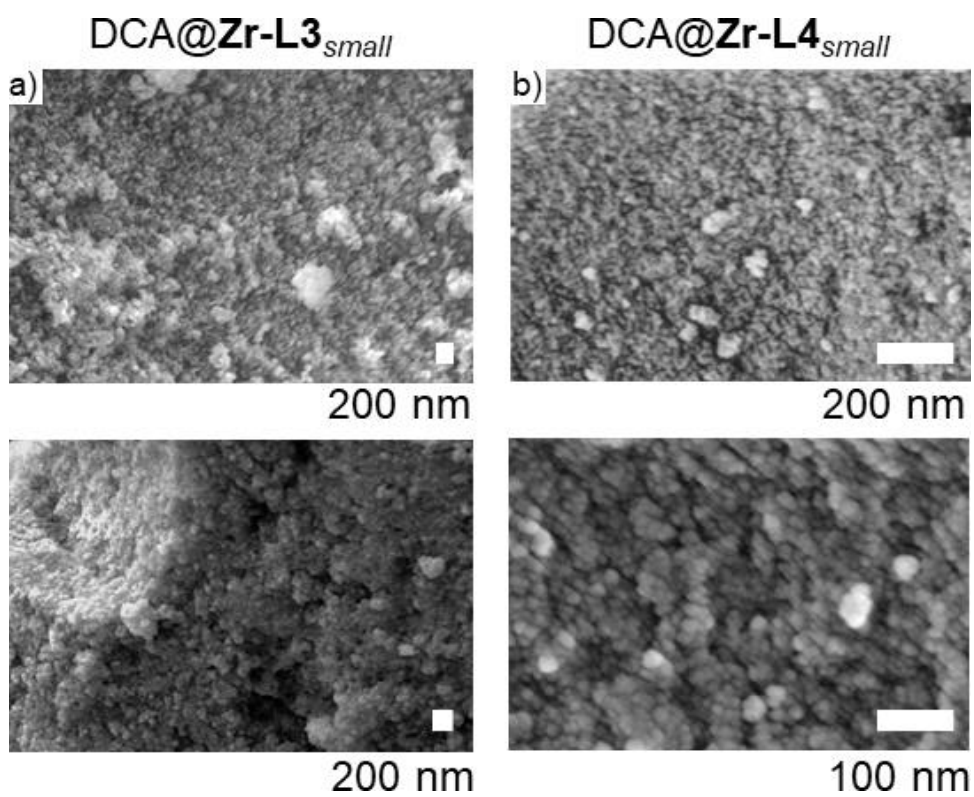


Figure S2. SEM images of a) DCA@Zr-L3_{small} and b) DCA@Zr-L4_{small}.

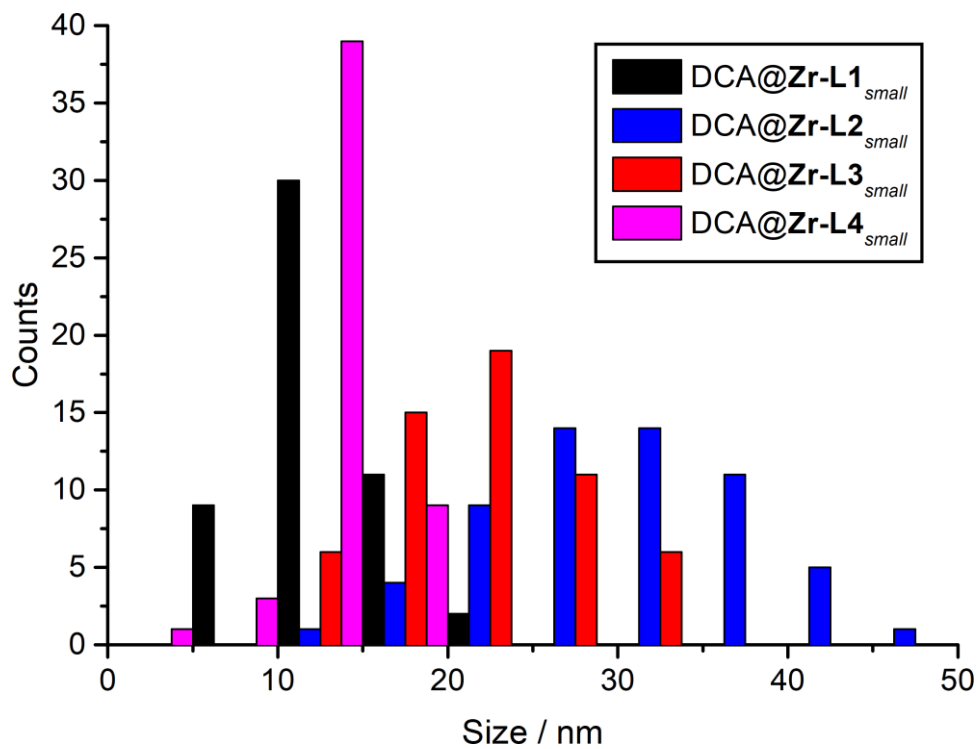


Figure S3. Particle size distribution histogram for DCA@Zr-LX_{small} samples.

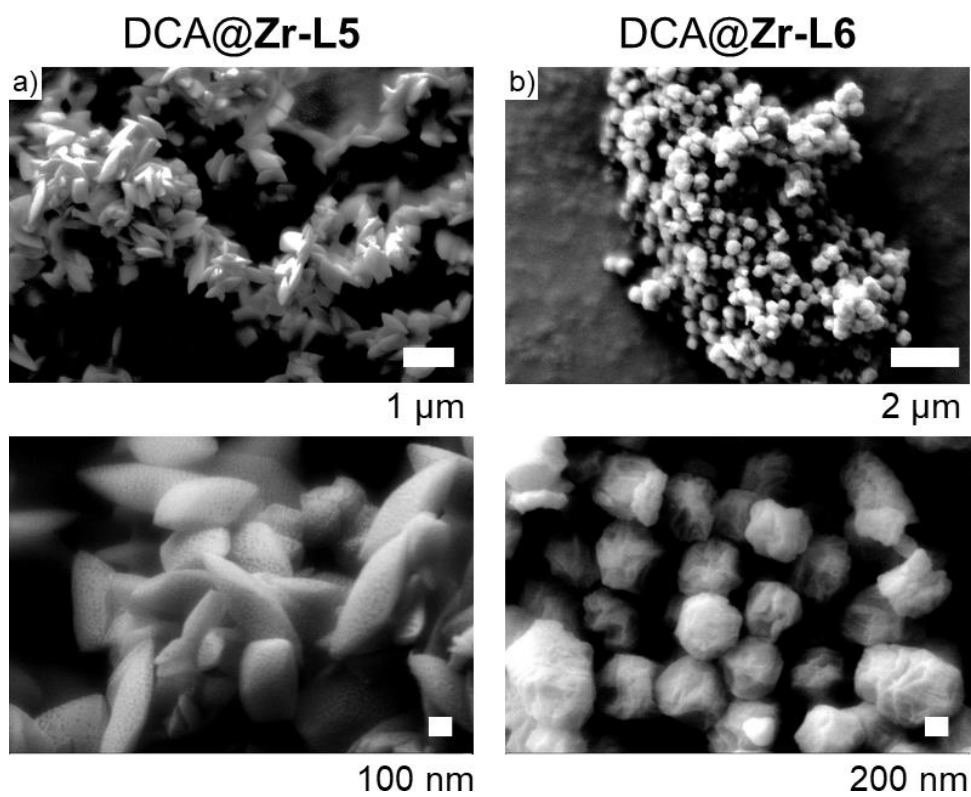


Figure S4. SEM images of a) DCA@Zr-L5 and b) DCA@Zr-L6.

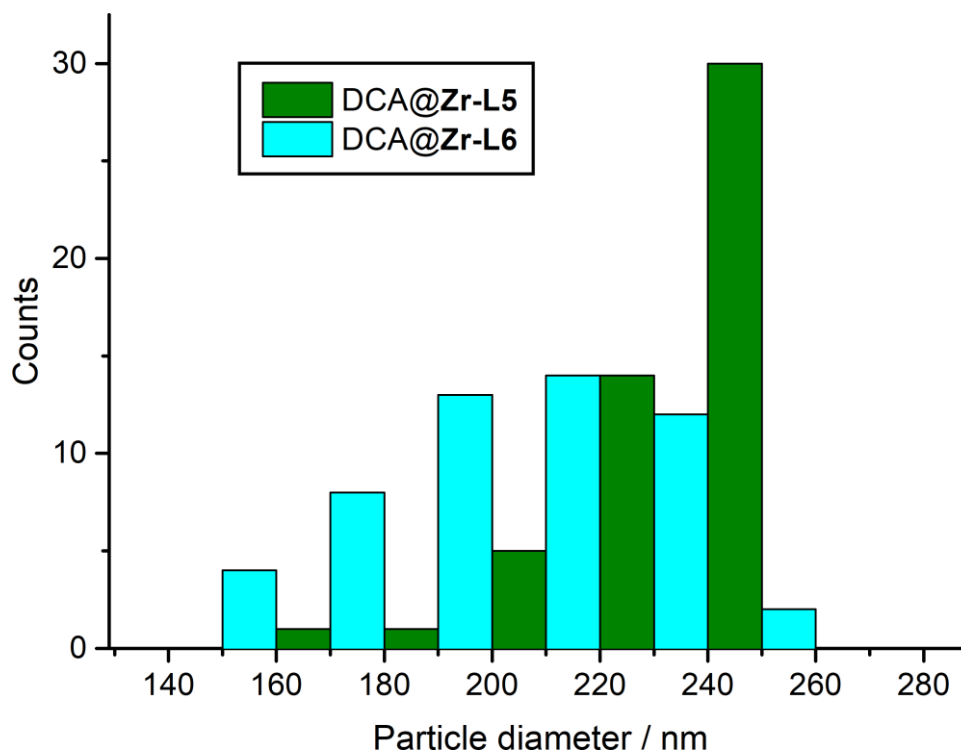


Figure S5. Particle size distribution histogram for DCA@Zr-L5 and DCA@Zr-L6.

Table S1. Average particle sizes of the MOFs synthesised using the ZrOCl_2 procedure

Sample	Particle diameter (nm)	Standard deviation (nm)
DCA@Zr-L1 _{small}	12.8	3.6
DCA@Zr-L2 _{small}	30.2	7.9
DCA@Zr-L3 _{small}	21.7	5.3
DCA@Zr-L4 _{small}	12.5	2.9
DCA@Zr-L5	232	30
DCA@Zr-L6	196	32

The porosity of the samples was determined by N_2 sorption/desorption isotherms. The four terephthalate MOFs present type IV isotherms (Figure S6) with H2 hysteresis loops, which are typical of interconnected networks of pores with different size and shape and suggest highly defective structures.^{S4} The fact that the hysteresis closes before 0.9 P/P_0 in all cases, in contrast to H3 hysteresis loops, which are typical of aggregates of particles, strongly suggests that the hierarchical porosity is a consequence of attachment of DCA modulators and resulting missing linker and cluster defects, although some contribution of inter-particle space should also be considered.

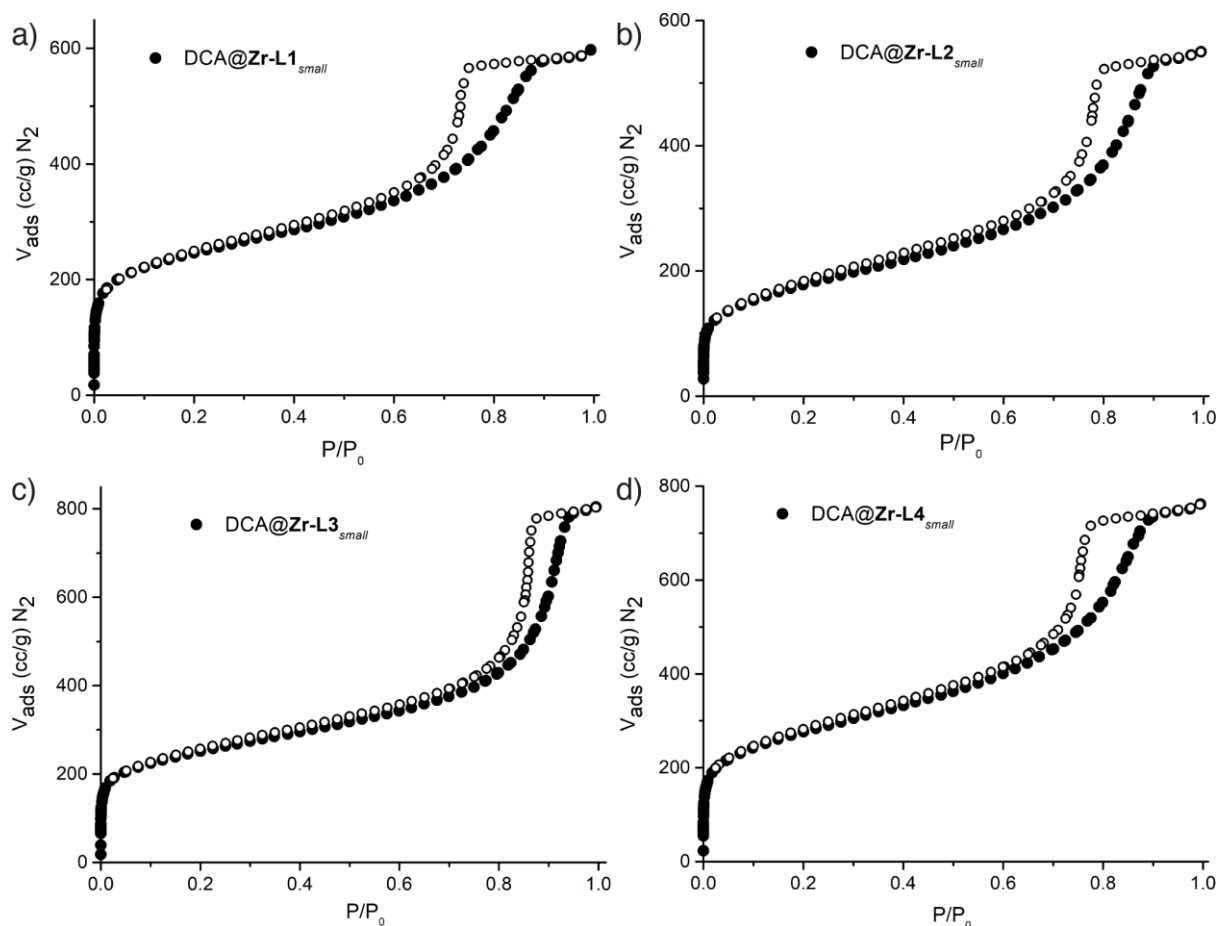


Figure S6. N₂ uptake isotherms (77 K) for a) DCA@Zr-L1_{small}, b) DCA@Zr-L2_{small}, c) DCA@Zr-L3_{small}, and d) DCA@Zr-L4_{small}. Filled symbols indicate adsorption, empty symbols desorption.

Comparison of the N₂ uptake isotherms with those of DCA@Zr-L5 and DCA@Zr-L6 (Figure S7) shows that while the uptakes in the micropore region for the small samples are lower than typical UiO-66 materials, the defectivity induces pore volumes similar to DCA@Zr-L6. This difference is also borne out in the pore size distributions (PSDs, Figure S8) which show well defined micropores of expected size for DCA@Zr-L5 and DCA@Zr-L6 but, broad flat profiles for the DCA@Zr-LX_{small} samples, showing the lack of micropore structure in the small nanoparticulate MOFs, with appreciable mesoporosity.

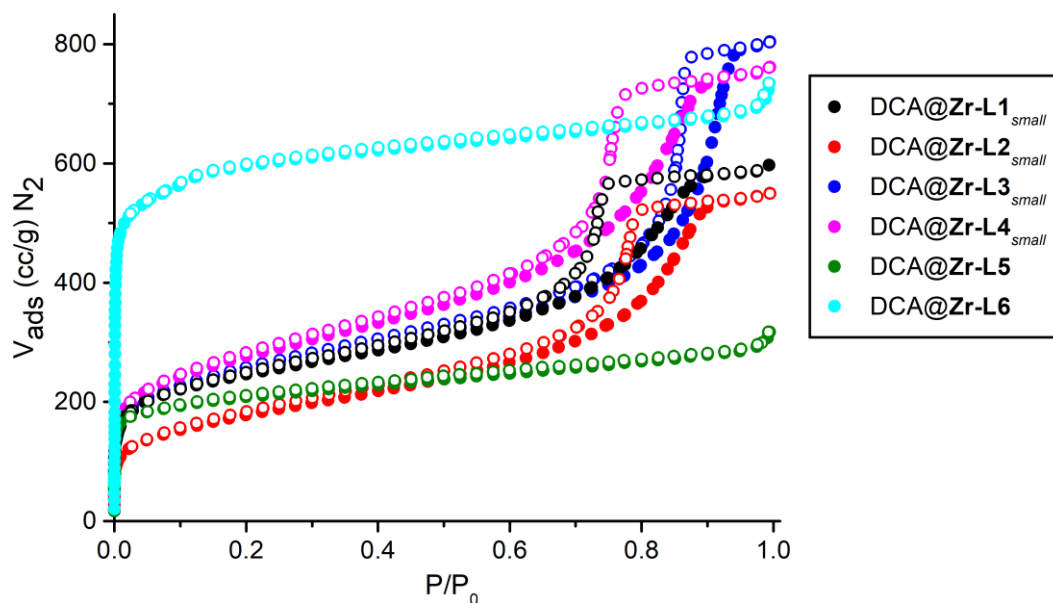


Figure S7. Comparison of N_2 uptake isotherms (77 K) for all the MOFs synthesised using the $ZrOCl_2$ protocol. Filled symbols indicate adsorption, empty symbols desorption.

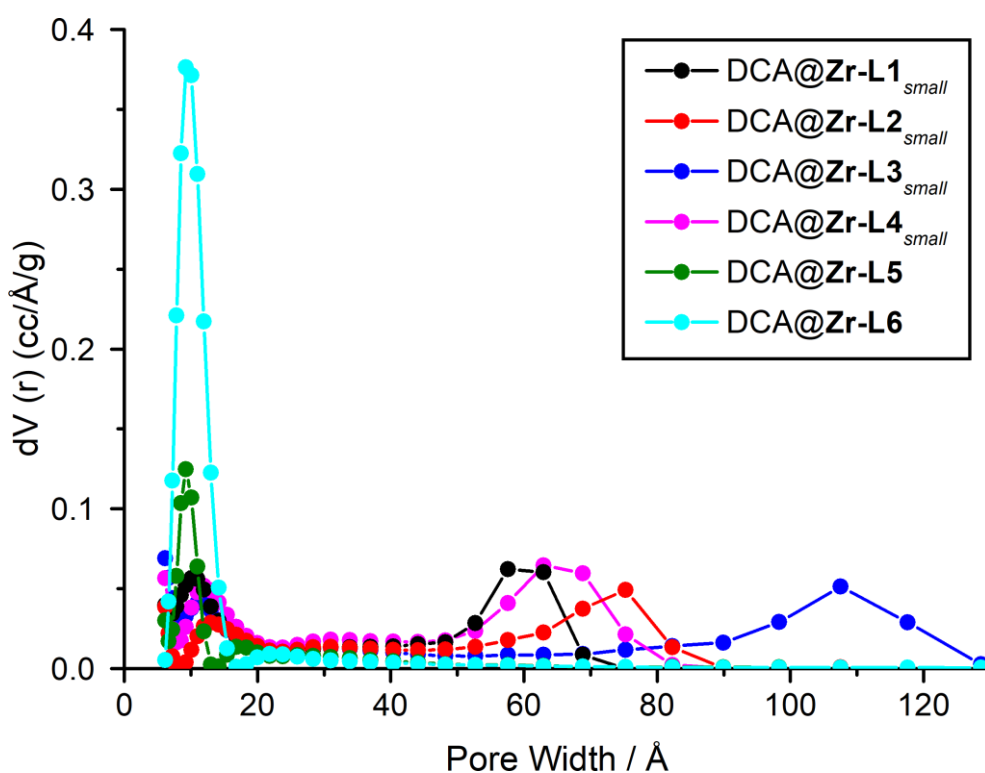


Figure S8. Pore size distributions, calculated from the N_2 uptake isotherms, of the MOFs synthesised by the $ZrOCl_2$ protocol, showing the mesopores of the defective $DCA@Zr-LX_{small}$ MOFs. N_2 on carbon at 77 K, slit pore, QSDFT, equilibrium model.

^1H Nuclear magnetic resonance (NMR) spectra of acid-digested samples of the DCA@MOFs ($\text{D}_2\text{SO}_4 / \text{DMSO-}d_6$) show significant quantities of DCA in all cases. The ^1H NMR spectrum for digested DCA@Zr-L1_{small} is shown as an exemplar in Figure S9; the resonance at $\delta = \sim 6.5$ ppm corresponds to the $-\text{CCl}_2\text{H}$ proton of DCA. It is not possible to quantitatively determine DCA loading values from the NMR spectra alone, as the exact composition of the MOF will depend on defectivity and the replacement of MOF linkers with capping DCA molecules. However, estimating the molar ratio of DCA compared to the ligand gives a qualitative assessment of the extent of DCA incorporation (Table S2).

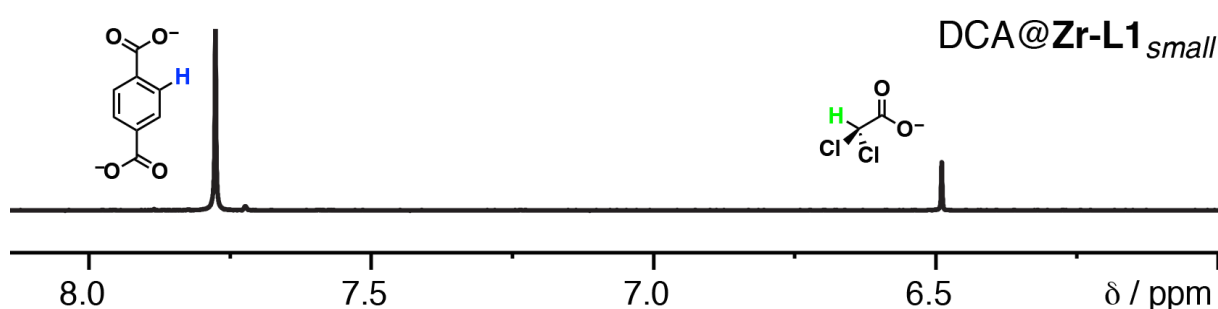


Figure S9. Partial ^1H NMR spectrum ($\text{D}_2\text{SO}_4 / \text{DMSO-}d_6$) of digested DCA@Zr-L1_{small}.

Table S2. Molar ratios of DCA incorporation from ^1H NMR spectra of acid digested samples of the DCA@MOFs.

Sample	DCA mol % to L
DCA@Zr-L1 _{small}	30.3
DCA@Zr-L2 _{small}	34.6
DCA@Zr-L3 _{small}	34.5
DCA@Zr-L4 _{small}	45.5
DCA@Zr-L5	34.1
DCA@Zr-L6	18.6

Fourier transform infrared (FTIR) spectra were collected for the MOFs and compared to those of empty analogues and DCA (Figure S10). FT-IR spectra of the DCA@MOFs show appearance of a new band in the carboxylic acid region, characteristic of DCA carboxylic acid, but shifted when compared to free DCA, possibly as a consequence of its attachment to Zr units. The presence of a new band associated to the C-Cl stretch (800 cm^{-1}) is appreciable with no shifting observed.

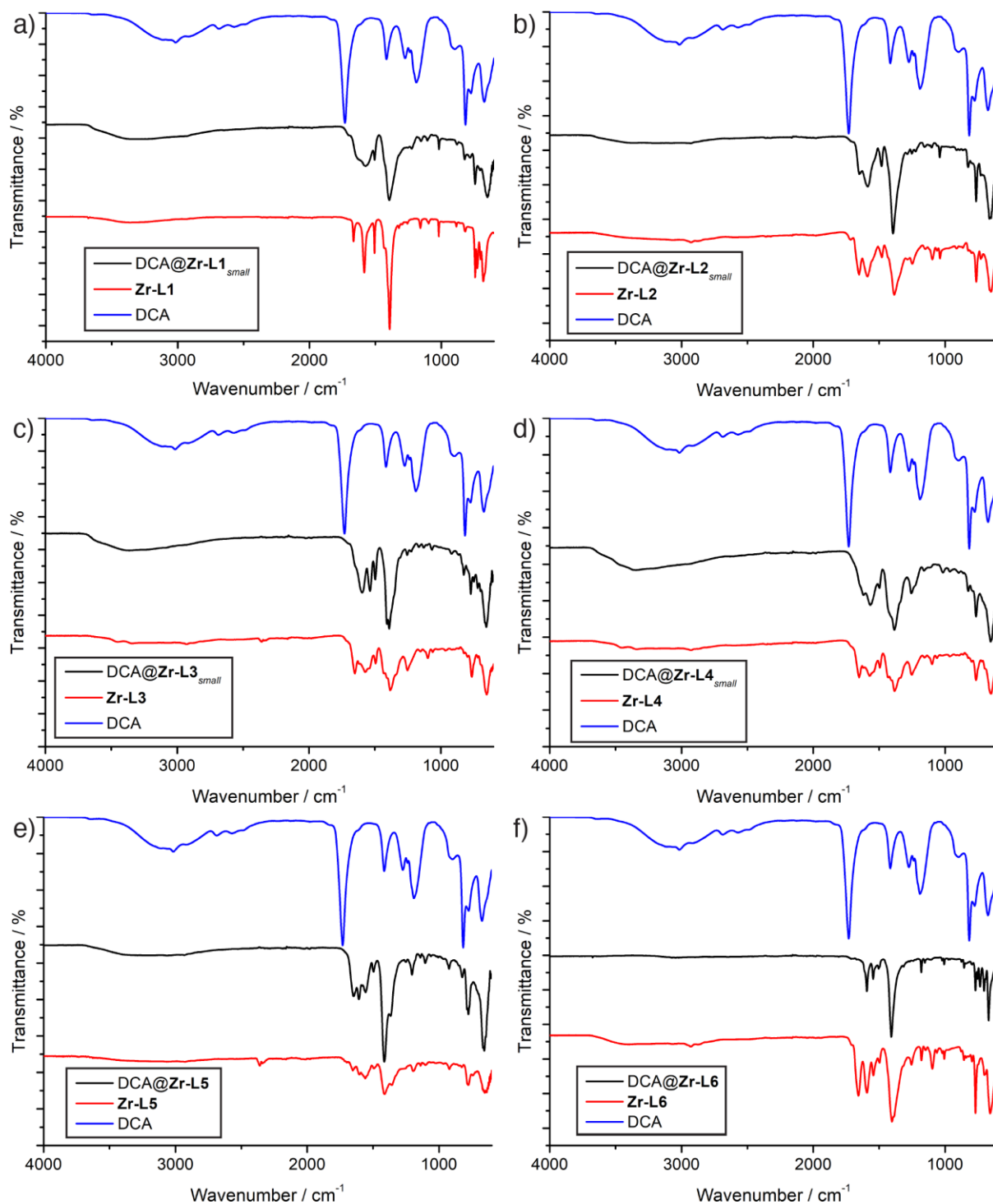


Figure S10. Comparison of FTIR spectra of DCA-loaded MOFs with the empty analogue and DCA for a) DCA@Zr-L1_{small}, b) DCA@Zr-L2_{small}, c) DCA@Zr-L3_{small}, d) DCA@Zr-L4_{small}, e) DCA@Zr-L5, and f) DCA@Zr-L6.

Thermogravimetric analysis (TGA) of the samples (Figure S11) shows mass loss events which are not characteristic of the NMOF structure itself, but of DCA thermal decomposition.

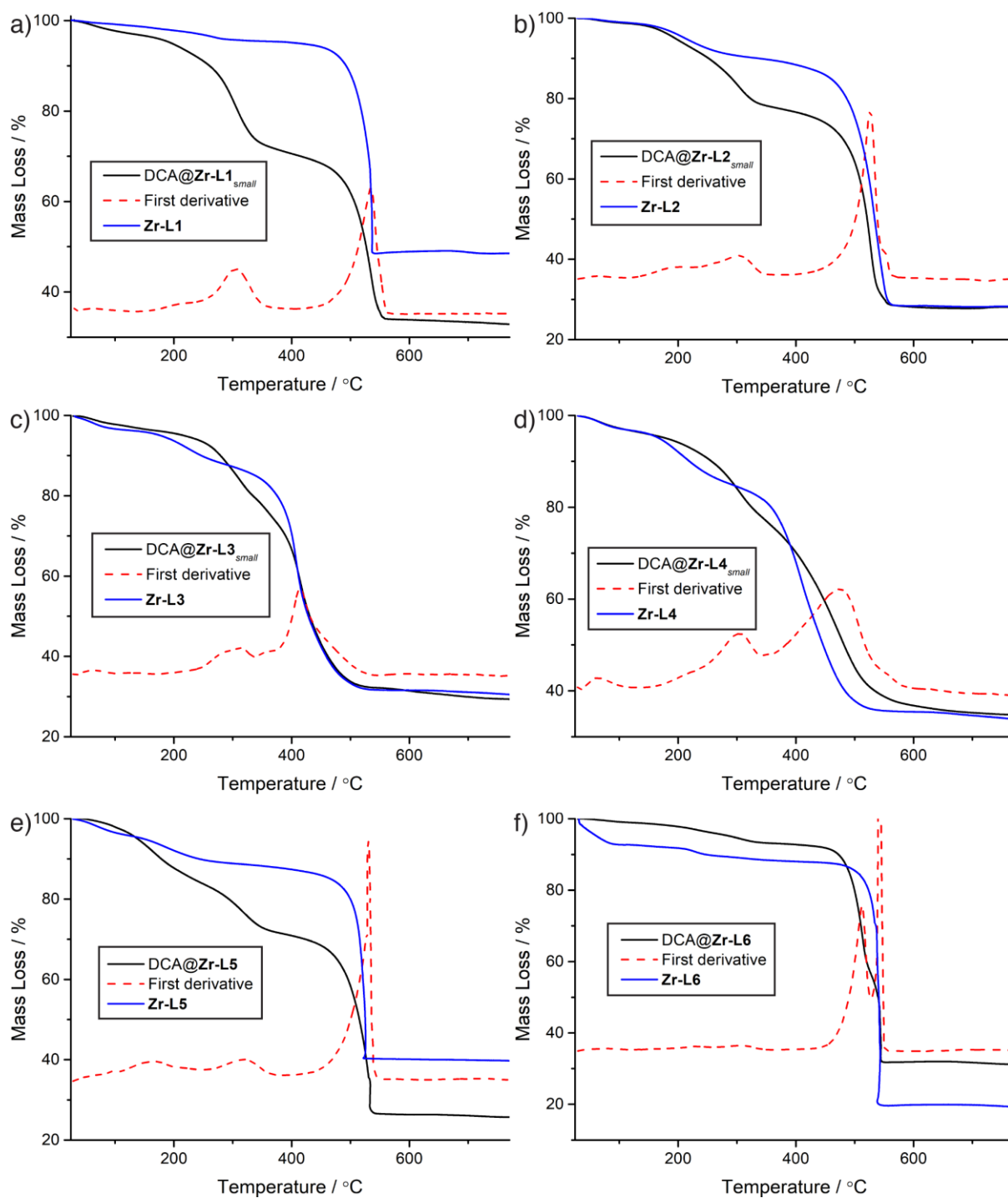


Figure S11. TGA traces in air of DCA loaded MOFs compared to empty MOFs for a) DCA@Zr-L1_{small}, b) DCA@Zr-L2_{small}, c) DCA@Zr-L3_{small}, d) DCA@Zr-L4_{small}, e) DCA@Zr-L5, and f) DCA@Zr-L6.

DCA mass loss events within the MOF occur at a higher temperature than free DCA thermal decomposition (198°C),^{S5} as a consequence of its attachment to the Zr clusters. Mass loss events occurring before 225 °C are characteristic of DMF incorporation and water loss from

the structure, which is observed for both empty and DCA-containing MOFs, more notably for empty MOFs, as DMF coming from the synthetic process can get incorporated to the Zr₆, as well as formic acid from DMF hydrolysis during the reaction.^{S2} However, DCA mass loss events from 250–375 °C can be easily identified in the trace and the first derivative, allowing DCA content to be quantified, and in agreement with the ¹H NMR spectra (Figure S9) and FTIR spectra (Figure S10) which also show DCA is present.

To investigate the composition of the materials, the theoretical mass loss attributed to both linker and DCA for different model structures, in which DCA displaces the linkers in the structure, was calculated (Table S3) and compared to the experimental thermal decomposition (Table S4). Note that this approximation simply substitutes one linker molecule for one DCA molecule (steric hindrance suggests it would not be possible for two DCA molecules to replace one terephthalate linker) and one OH⁻ to charge balance. This model does not account for missing linker or cluster defects or other deviations from an ideal structure.

Table S3. Theoretical compositions of different defective UiO-66 samples.

$$\text{Linker wt\%} = \frac{(x - y)L}{\text{Zr}_6\text{O}_4(\text{OH})_4\text{L}(x - y)(\text{DCA})_y(\text{OH})_y} * 100$$

$$\text{DCA wt\%} = \frac{y\text{DCA}}{\text{Zr}_6\text{O}_4(\text{OH})_4\text{L}(x - y)(\text{DCA})_y(\text{OH})_y} * 100$$

Linker :DCA	DCA@Zr-L1		DCA@Zr-L2		DCA@Zr-L3		DCA@Zr-L4		DCA@Zr-L5		DCA@Zr-L6	
	L1	DCA	L2	DCA	L3	DCA	L4	DCA	L5	DCA	L6	DCA
5:1	49.9	7.8	59.6	6.3	55.9	6.8	52.1	7.4	56.5	6.8	59.3	6.3
4:2	40.4	15.7	50.1	13.2	46.3	14.2	42.5	15.2	46.9	14.0	49.8	13.3
3:3	30.6	23.9	39.6	20.8	36.0	22.0	32.5	23.2	36.6	21.8	39.3	20.9

Table S4: Analysis of experimental TGA profiles

Sample	% Linker TGA	% DCA TGA
DCA@Zr-L1 _{small}	32.3	26.2
DCA@Zr-L2 _{small}	45.5	19.3
DCA@Zr-L3 _{small}	37.7	21.5
DCA@Zr-L4 _{small}	34.9	26.4
DCA@Zr-L5	46.7	14.1
DCA@Zr-L6	60.1	6.55

The experimental DCA and linker mass loss (Table S4) correlate well with the theoretical composition $[\text{Zr}_6\text{O}_4(\text{OH})_4(\text{L})_3(\text{DCA})_3(\text{OH})_3]_n$ in the case of the DCA-loaded terephthalate MOFs, while DCA@**Zr-L5** is closer to $[\text{Zr}_6\text{O}_4(\text{OH})_4(\text{L})_4(\text{DCA})_2(\text{OH})_2]_n$ and DCA@**Zr-L6** to $[\text{Zr}_6\text{O}_4(\text{OH})_4(\text{L})_5(\text{DCA})_1(\text{OH})_1]_n$, meaning that the terephthalate derivatives are considerably more defective, as was also suggested by PXRD and N_2 adsorption analyses.

S3. Synthesis of DCA@MOFs of Larger Size

DCA@UiO-66 derivatives synthesis was performed following the former coordination modulation protocol, using a 1:1 ratio of $ZrCl_4$ and linker and adding 10 equivalents of DCA instead to the syntheses, together with 1 equivalent of HCl. After 24 hours, the reaction mixtures were cooled to room temperature and the NMOFs were collected with centrifugation and washed with DMF (x1) and MeOH (x3) by dispersion centrifugation cycles.

PXRD patterns (Figure S12) show highly crystalline and phase pure MOFs with the UiO-66 topology.

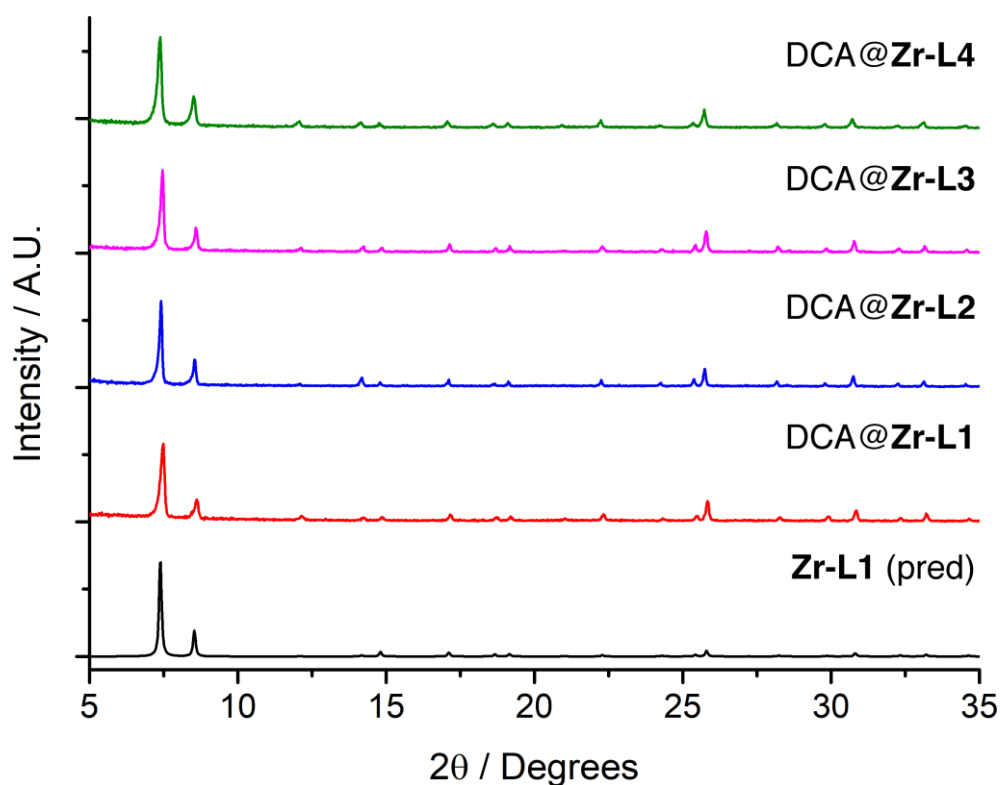


Figure S12. Stacked PXRD patterns of the larger terephthalate MOFs, DCA@Zr-L1 – DCA@Zr-L4, compared to the predicted pattern for Zr-L1.

SEM imaging (Figures S13 and S14) showed the particles to be around 75-150 nm in diameter, with particle size distributions (Figure S15) showing that DCA@Zr-L1 and DCA@Zr-L4 are slightly smaller than DCA@Zr-L2 and DCA@Zr-L3. Particle size data is presented in Table S5.

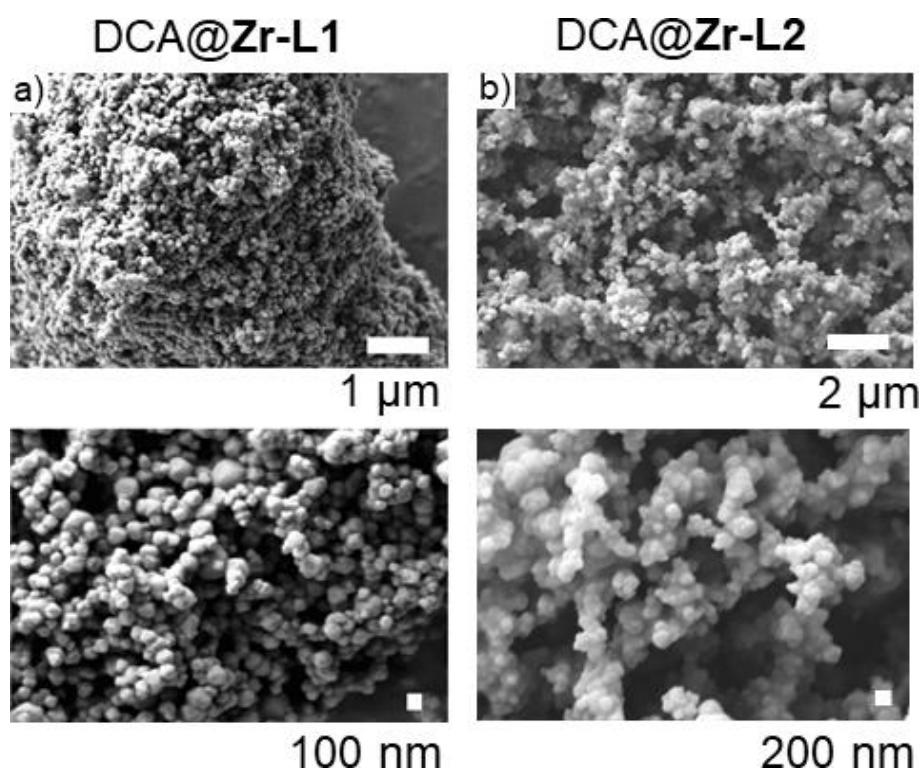


Figure S13. SEM images of a) DCA@Zr-L1 and b) DCA@Zr-L2.

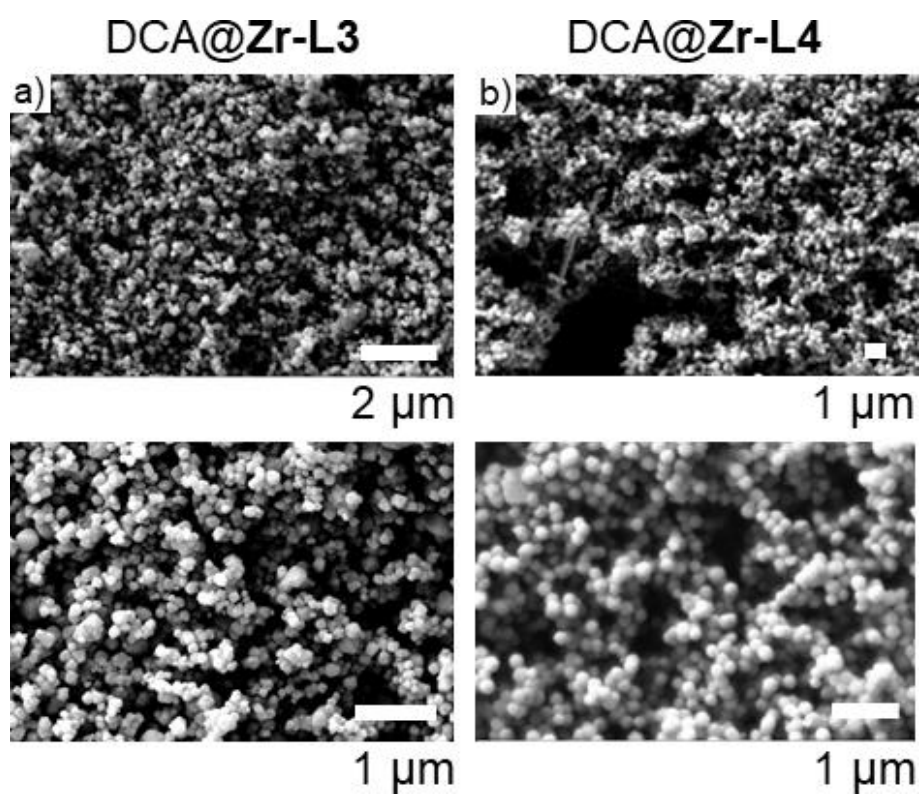


Figure S14. SEM images of a) DCA@Zr-L3 and b) DCA@Zr-L4.

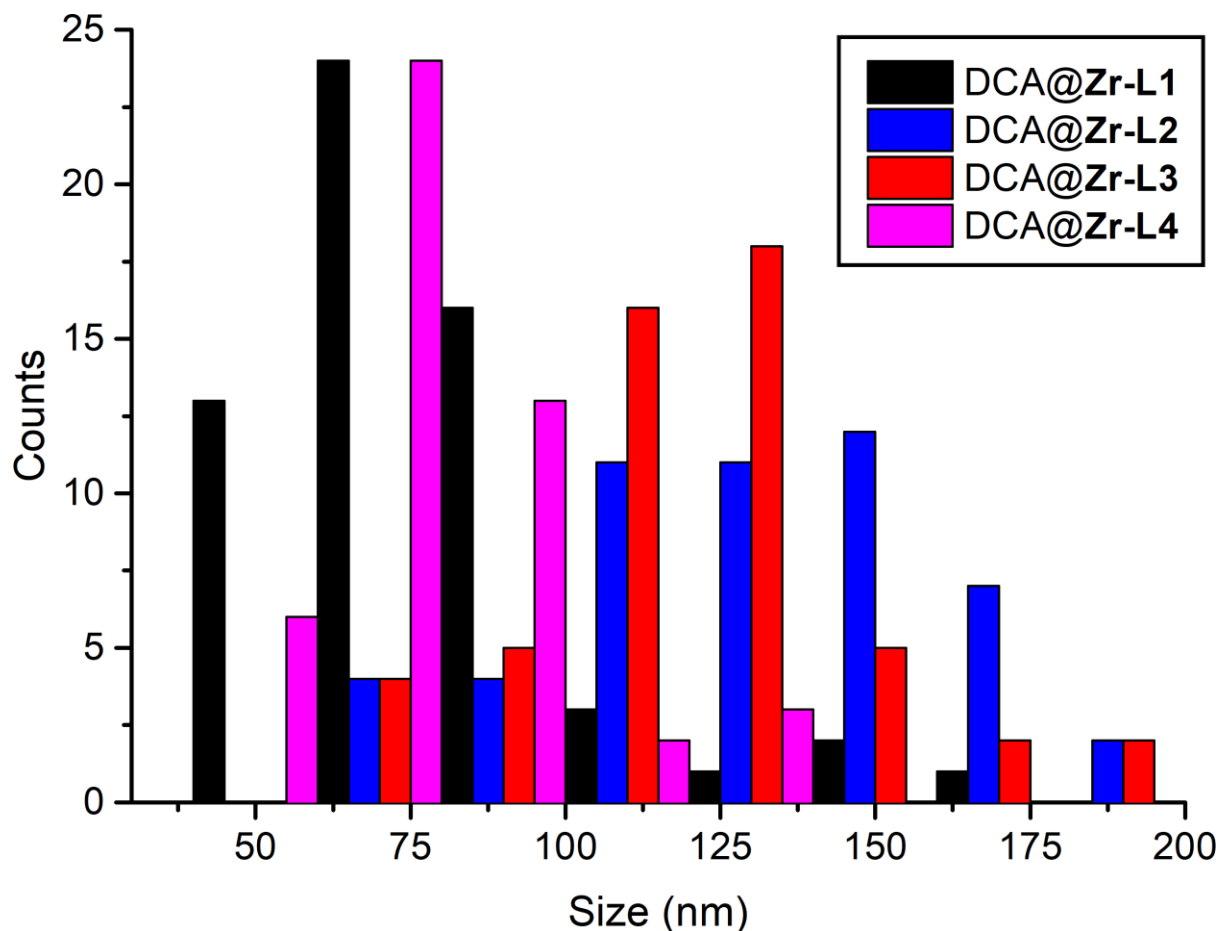


Figure S15. Particle size distribution histogram for the larger DCA-loaded terephthalate MOF samples.

The samples' porosity was analysed by N_2 adsorption and desorption measurements (Figure S16), which ultimately confirmed DCA incorporation through binding to the Zr_6 clusters, as the samples present higher BET surface areas and pore volumes (Table S5) than those previously reported in the literature for pristine materials,^{S6} as consequence of DCA incorporation. In fact, DCA@Zr-L1 has a surface area of $1510 \text{ m}^2\text{g}^{-1}$ and a pore volume of 0.76 ccg^{-1} , while pristine non-defective Zr-L1 has a BET surface area of $1200 \text{ m}^2\text{g}^{-1}$ and pore volume of 0.4 ccg^{-1} .^{S7} The pore size distributions show defective pores (Figure S17), again as a consequence of DCA attachment and defect induction.

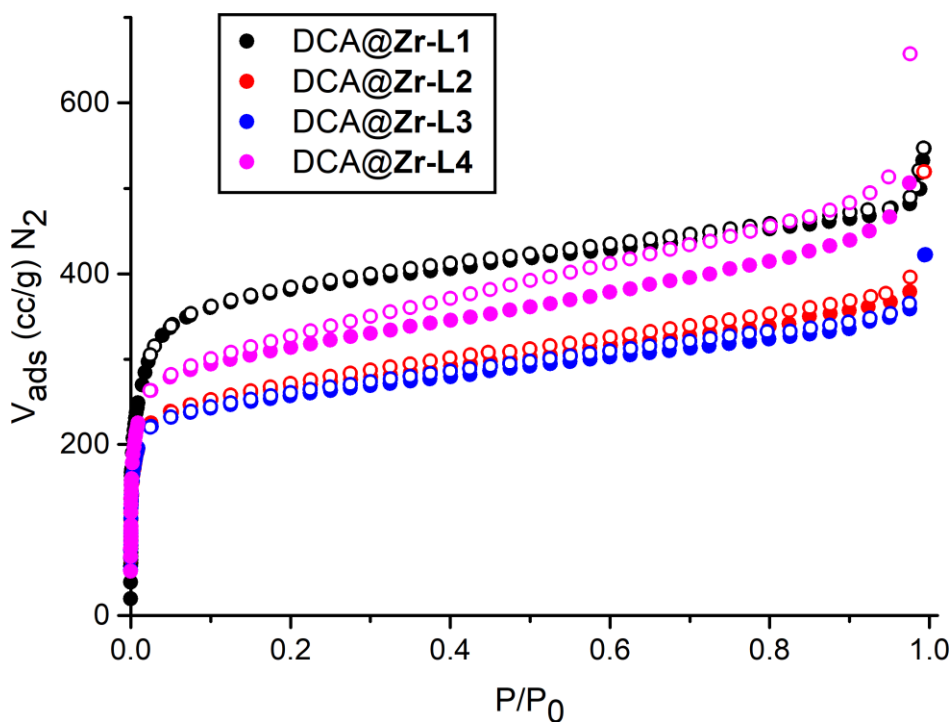


Figure S16. Comparison of N_2 uptake isotherms (77 K) for larger DCA-loaded terephthalate MOF samples. Filled symbols indicate adsorption, empty symbols desorption.

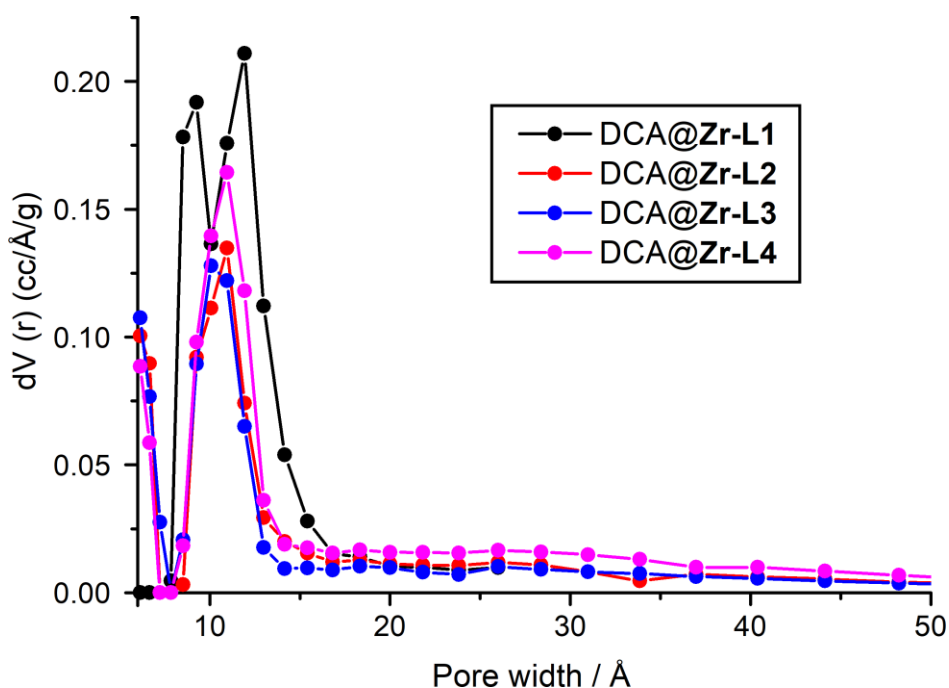


Figure S17. Pore size distributions, calculated from the N_2 uptake isotherms, for larger DCA-loaded terephthalate MOFs, showing the expected pores for UiO-66 samples but with some larger, defect-based pores. N_2 on carbon at 77 K, slit pore, QSDFT, equilibrium model.

^1H NMR spectra of the acid digested samples again show high DCA incorporation (ca. 30 mol % compared to linker) but lower than in the case of the smaller analogue MOFs. A comparison between the spectra of $\text{DCA@Zr-L1}_{\text{small}}$ and DCA@Zr-L1 is given in Figure S18, where the resonance for the DCA $-\text{CCl}_2\text{H}$ proton is clearly smaller for the larger sample.

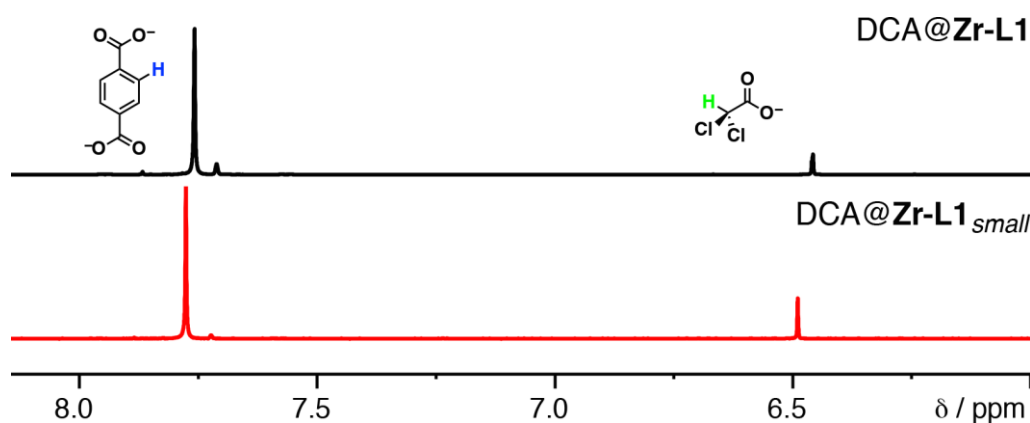


Figure S18: Partial stacked ^1H NMR spectra (D_2SO_4 / $\text{DMSO-}d_6$) of digested $\text{DCA@Zr-L1}_{\text{small}}$ (red) and DCA@Zr-L1 (black), showing the higher relative intensity of DCA for the smaller analogue MOF.

In great agreement with the smaller analogues, the FT-IR spectra of the DCA@Zr-LX MOFs (Figure S19) show vibration bands characteristic of DCA.

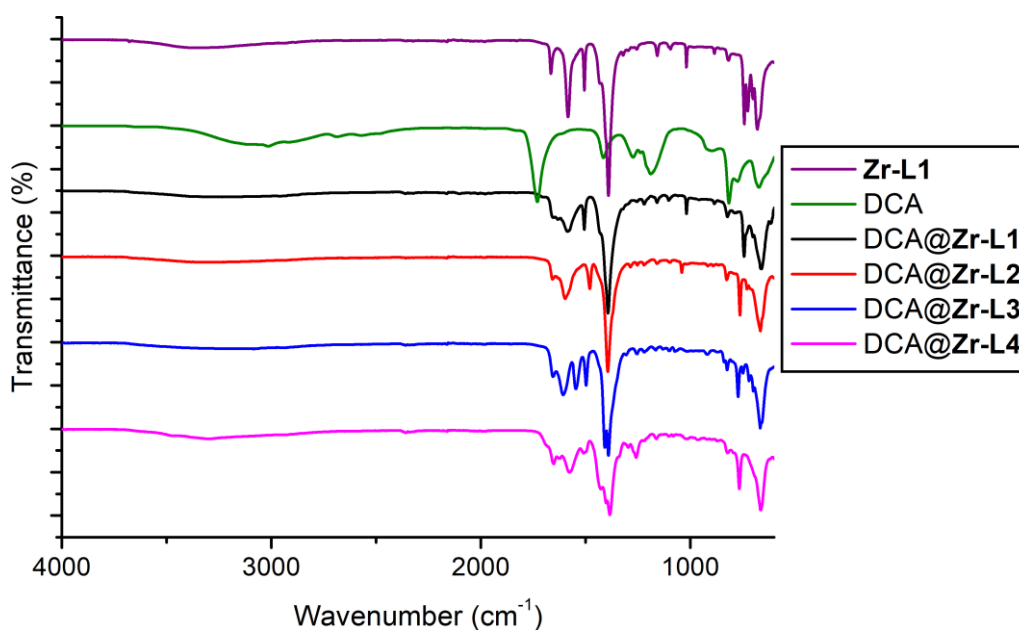


Figure S19. Stacked FT-IR spectra of the larger DCA-loaded terephthalate MOFs compared to empty Zr-L1 and DCA.

The carboxylic acid region shows less defined bands and appearance of new ones, possibly as a consequence of DCA attachment to the Zr_6 units. The presence of a new band associated to the C-Cl stretch (800 cm^{-1}) is appreciable in all samples.

TGA analysis enabled quantification of DCA loading and an estimation of the structural composition. A comparison of the TGA traces for the four DCA@Zr-terephthalate MOFs with an empty Zr-terephthalate MOF can be found in Figure S20.

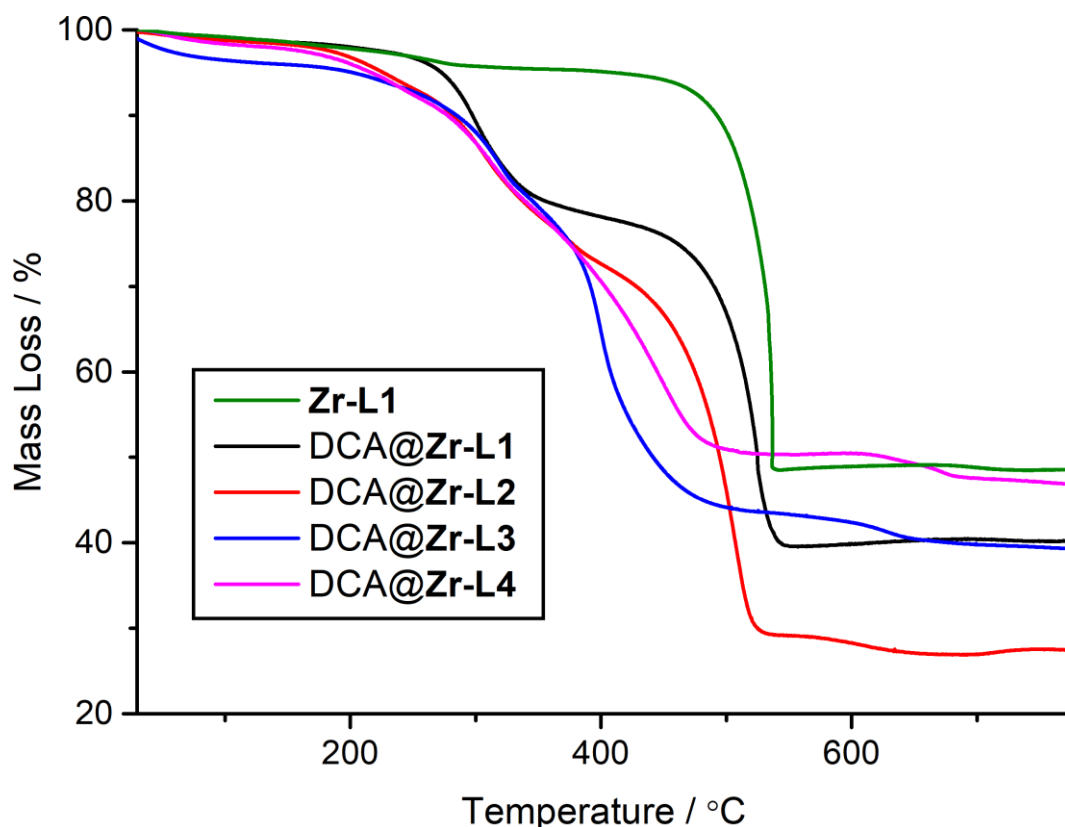


Figure S20. Comparison of the TGA profiles of the DCA@Zr-terephthalate MOFs with empty DCA@Zr-terephthalate.

Individual TGA profile representations for each sample are given in Figure S21, where DCA decomposition is inherently clear (ca. $250\text{--}375^\circ\text{C}$), and the estimated DCA content in weight percent is given in Table S6. The experimental DCA and linker mass losses were compared to those calculated for theoretical model structures where DCA replaces linkers (Table S3), in each case being close to the theoretical structure $[Zr_6O_4(OH)_4(L)_4(DCA)_2(OH)_2]_n$, indicating less defective structures than the smaller analogues (see Table S4). DCA Loadings are given in Table S5.

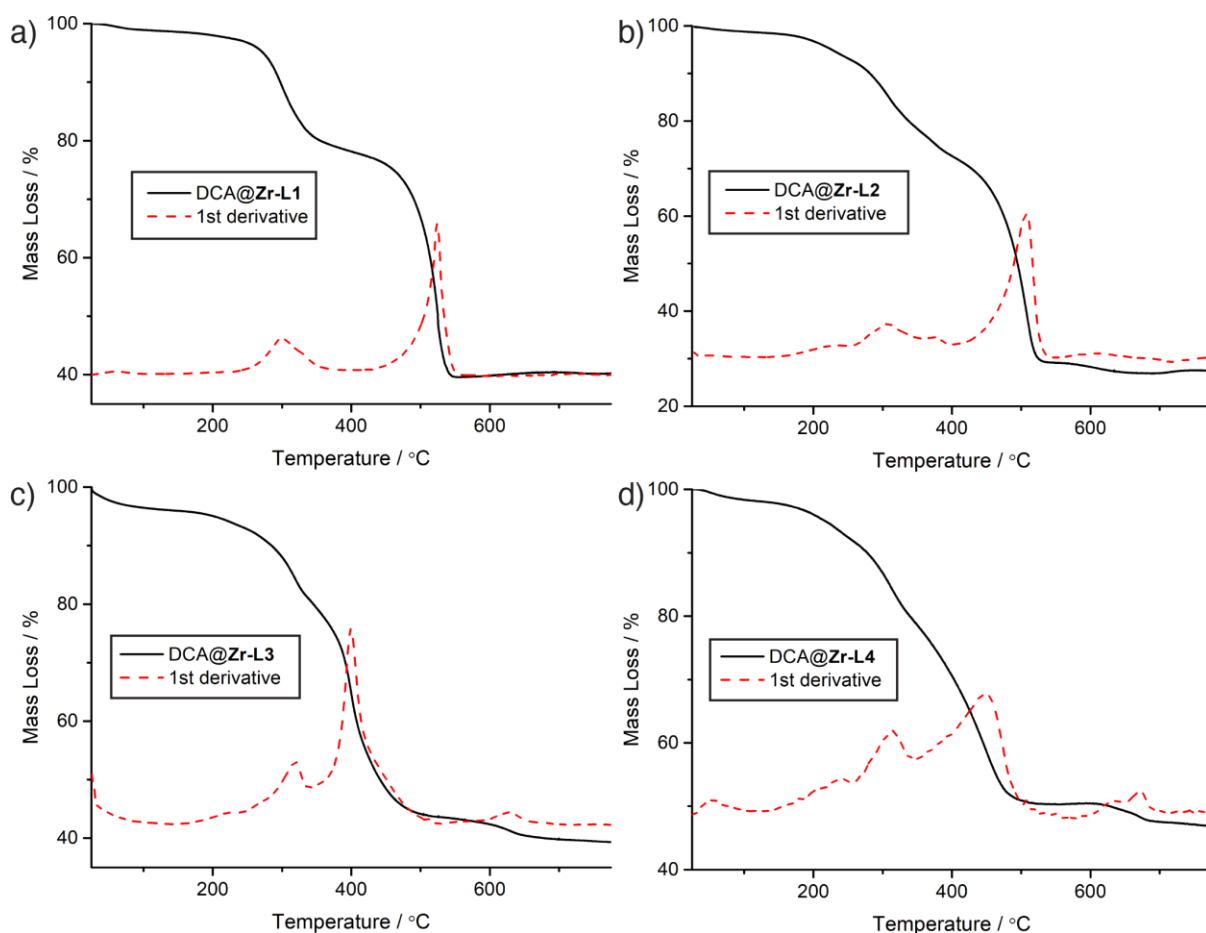


Figure S21. TGA profiles of the larger DCA-loaded terephthalate MOFs, showing DCA decomposition in the structure.

Table S5. Pertinent physical properties of the larger DCA-loaded terephthalate MOFs.

Sample	Size / nm	% DCA w/w	BET SA / m ² g ⁻¹	Pore volume / ccg ⁻¹
DCA@Zr-L1	77 ± 24	17.2	1510	0.76
DCA@Zr-L2	131 ± 30	16.7	1016	0.56
DCA@Zr-L3	121 ± 27	16.2	985	0.52
DCA@Zr-L4	81 ± 26	16.9	1189	0.83

Table S6. Analysis of experimental TGA profiles

Sample	% Linker TGA	% DCA TGA
DCA@Zr-L1	42.4	17.2
DCA@Zr-L2	50.3	16.7
DCA@Zr-L3	43.5	16.2
DCA@Zr-L4	38.2	16.9

S4. Colloidal Stability of DCA@MOFs

The particle size, aggregation and colloidal dispersion of the MOFs in water were measured by dynamic light scattering (DLS). In a scintillation vial, dispersion of the samples with a concentration of 0.1 mg mL^{-1} were prepared by sonication for 5 minutes prior to measurement. Each measurement consisted of 3 separated records, with a waiting time of 5 seconds. Each recording consisted of 14 runs, and no stirring was provided during the course of the experiment. The profiles for the small terephthalate nanoparticles are shown in Figure S22.

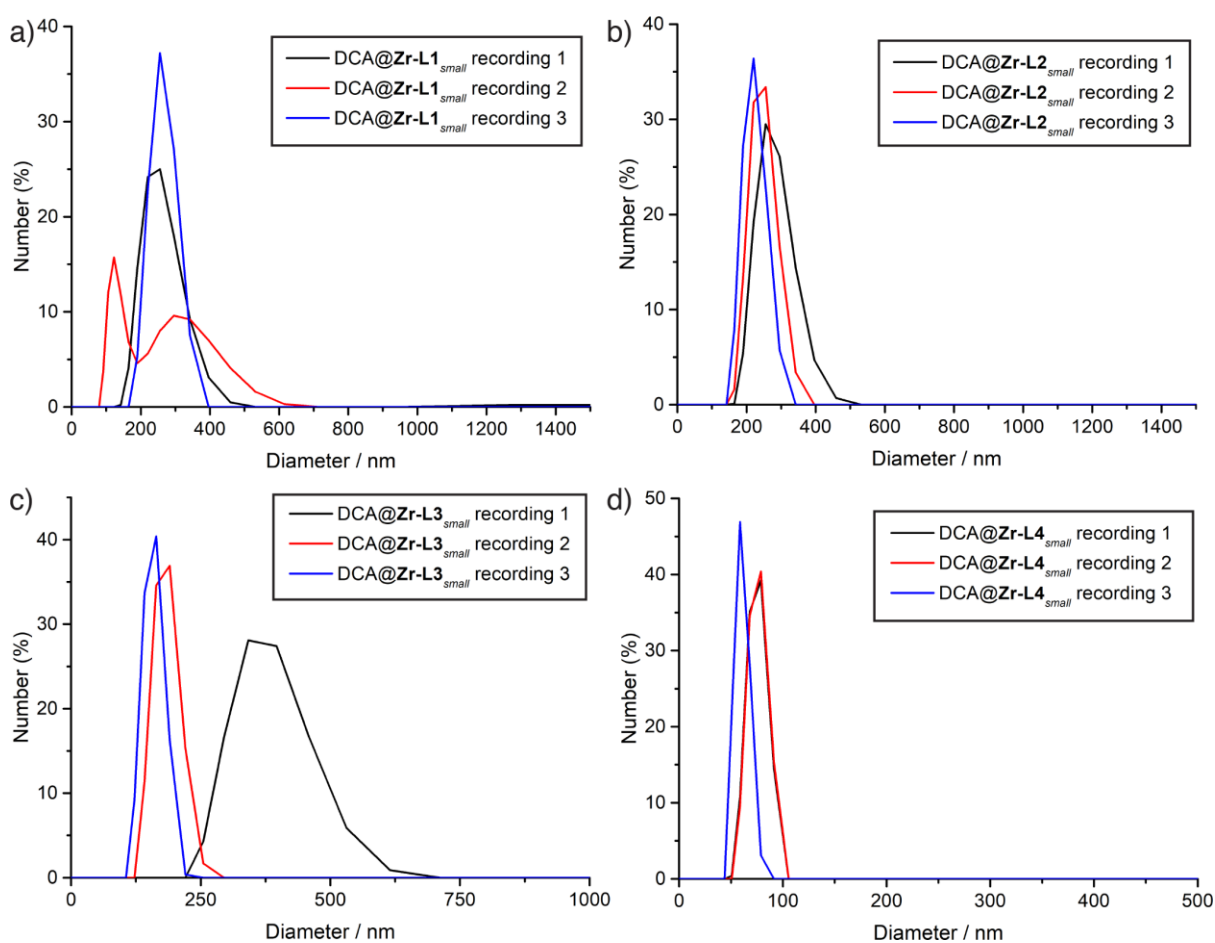


Figure S22. DLS profiles in water for a) DCA@Zr-L1_{small}, b) DCA@Zr-L2_{small}, c) DCA@Zr-L3_{small}, and d) DCA@Zr-L4_{small}.

The samples show a small degree of aggregation, except for DCA@Zr-L4_{small} which shows very little aggregation, likely due to positive charge on the pendant amino groups of L4 resulting in interparticle repulsion. The DLS profiles for DCA@Zr-L5 and DCA@Zr-L6 are shown in Figure S23, and also show only a small degree of aggregation.

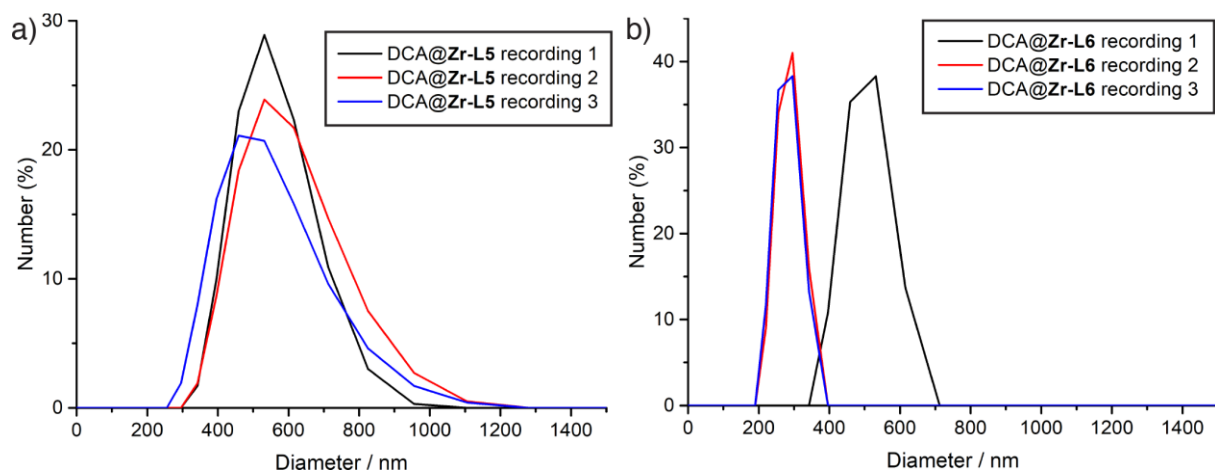


Figure S23. DLS profiles in water for a) DCA@Zr-L5 and b) DCA@Zr-L6.

Comparison of all samples (Figure S24) shows the difference in behaviour of the smaller and larger samples.

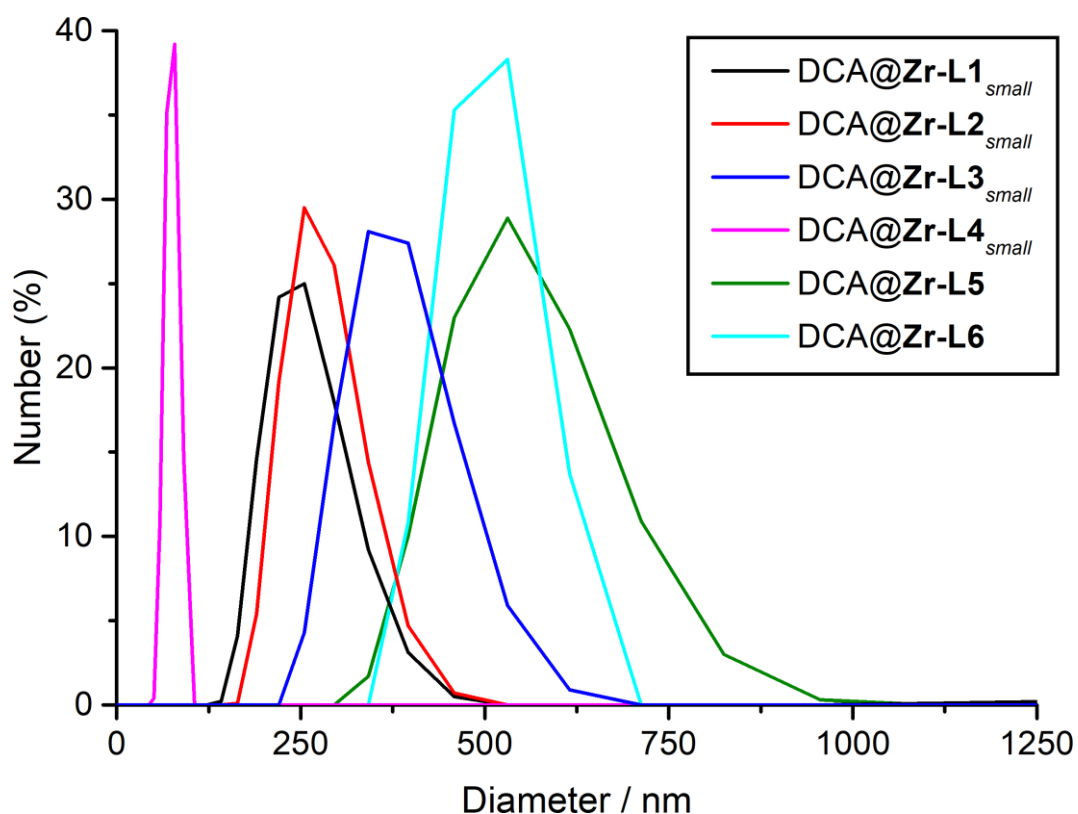


Figure S24. Comparison of the first recordings in the DLS experiments for aqueous suspensions of all the MOFs synthesised using the $ZrOCl_2$ protocol.

The larger DCA-loaded terephthalate MOFs were also well-dispersed in water, with only minor aggregation, showing size distributions (Figure S25) close to those determined by SEM.

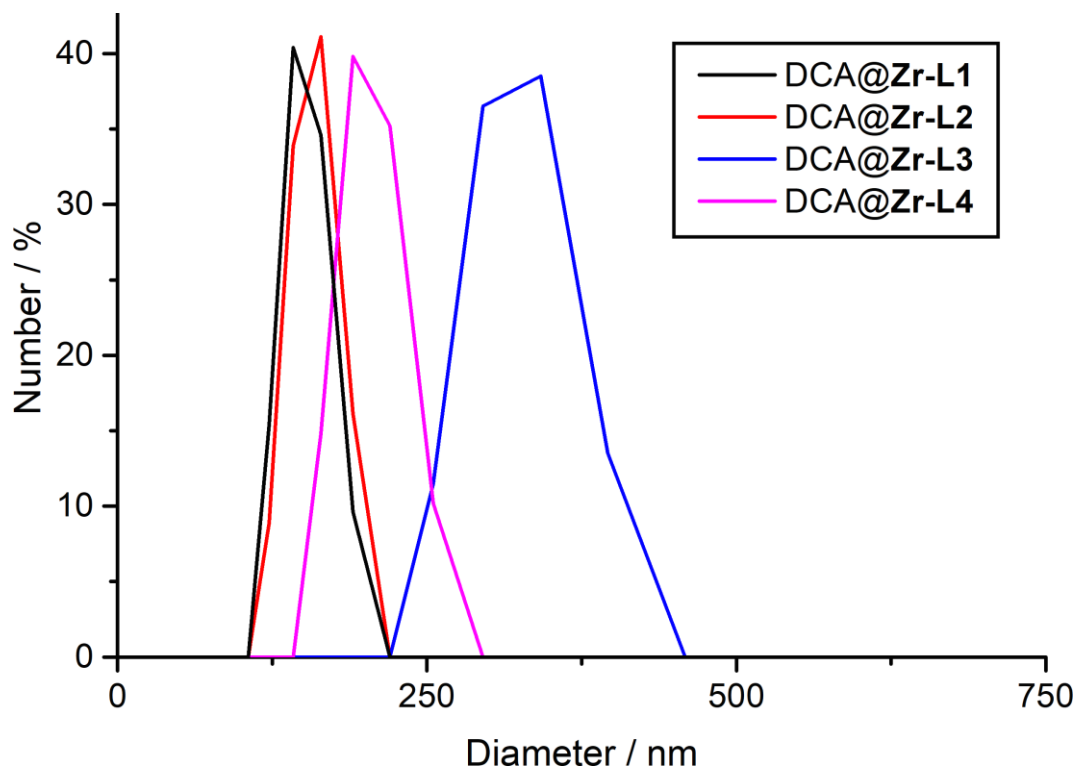


Figure S25. Comparison of the first recordings in the DLS experiments for aqueous suspensions of the larger DCA-loaded terephthalate MOFs.

It is expected that in biological systems, formation of a protein corona will limit any aggregation.^{S8,S9} To examine this, DLS experiments were carried out on the samples that showed some aggregation – the smaller terephthalate MOFs as well as **Zr-L5** and **Zr-L6** – when dispersed in phosphate buffered saline (PBS, pH = 7.4) that had been “spiked” with 2% w/w bovine serum albumin (BSA), to mimic biological conditions. All samples showed less aggregation and improved colloidal stability, and are compared with the analogous experiments in water in Figures S26 and S27. The smaller samples stabilised to around 100-150 nm aggregates, while DCA@**Zr-L4**_{small} appeared to be monodisperse and correlated well with particle sizes determined by SEM. The amino functionality of L4 is expected to be protonated under these conditions, and so likely forms a highly stable corona with the negatively charged BSA. The larger particles also formed stable dispersions close to the particle sizes determined by SEM, indicating that the MOFs will not be significantly aggregated during *in vitro* cytotoxicity studies.

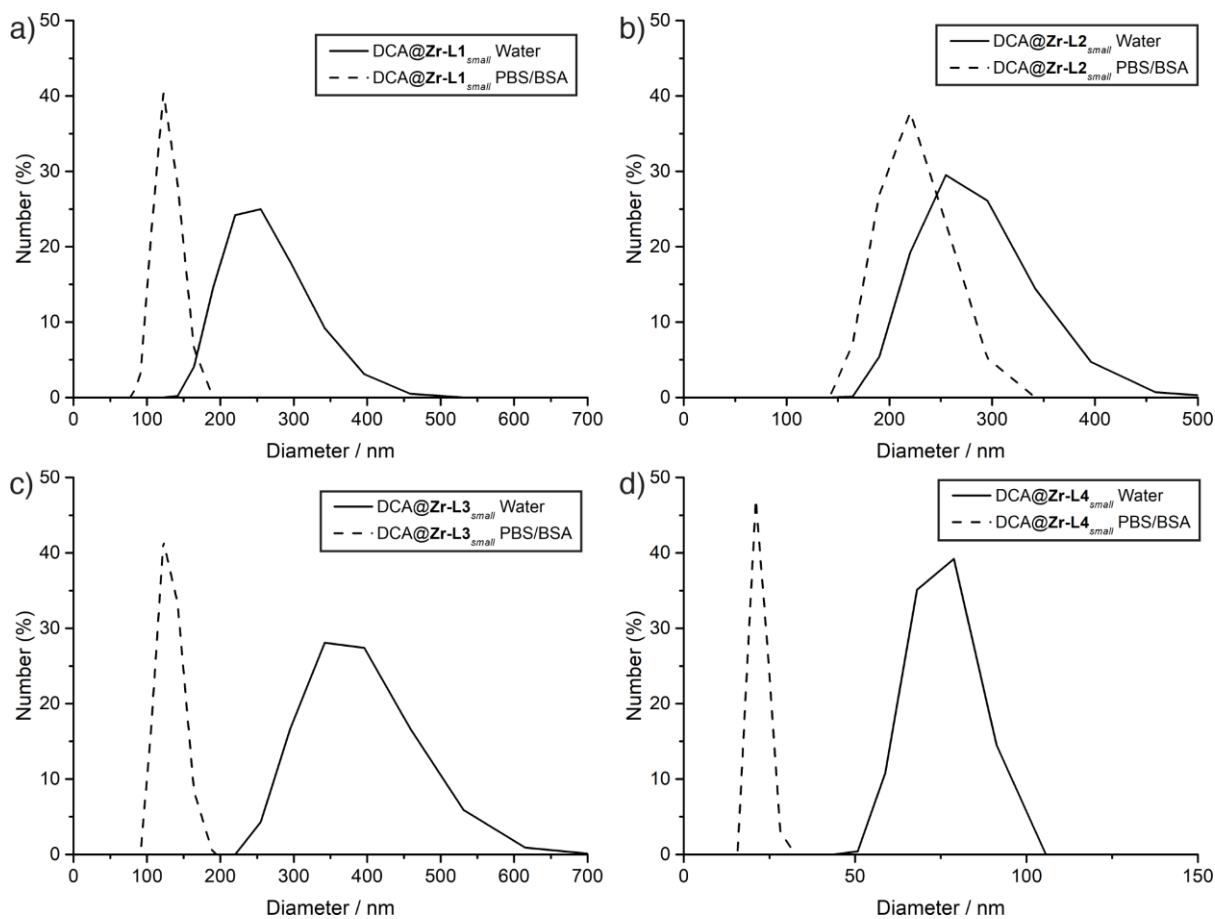


Figure S26. Comparison of the DLS profiles collected in water with those in 2% w/w BSA in PBS for a) DCA@Zr-L1_{small}, b) DCA@Zr-L2_{small}, c) DCA@Zr-L3_{small}, and d) DCA@Zr-L4_{small}.

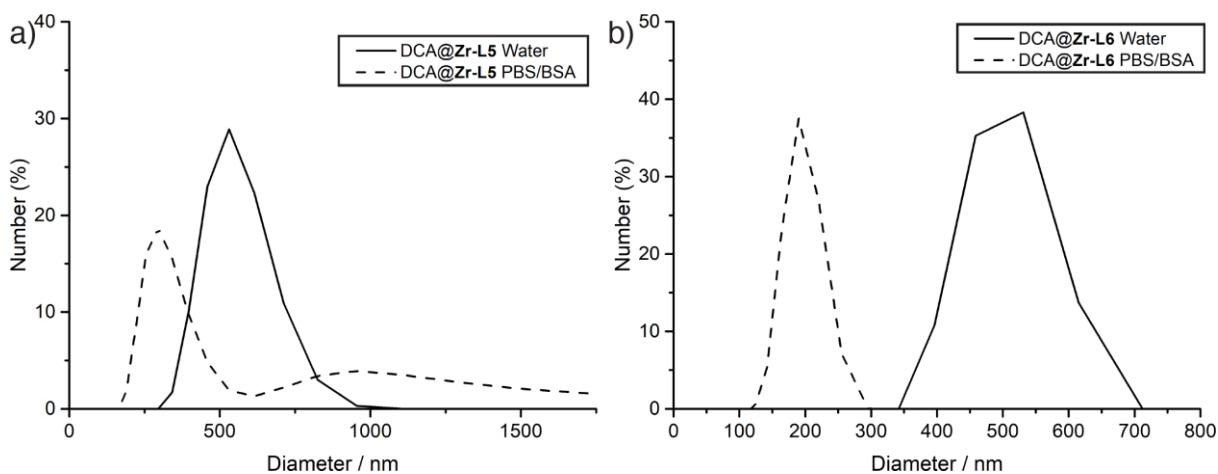


Figure S27. Comparison of the DLS profiles collected in water with those in 2% w/w BSA in PBS for a) DCA@Zr-L5 and b) DCA@Zr-L6.

S5. Therapeutic Efficiency of DCA@MOFs

The cytotoxicity of the DCA@MOFs and free DCA (in the form of sodium dichloroacetate, NaDCA, to negate cytotoxic effects of changing pH) was measured against MCF-7 breast carcinoma cells using the 3-(4,5-dimethylthiazol-2-yl)-5-(3-carboxymethoxyphenyl)-2-(4-sulfophenyl)-2H-tetrazolium (MTS, Promega, UK) reduction assay.

MCF-7 cells were maintained at 37 °C with 5% CO₂ in high rich glucose (4500 mgL⁻¹) Dulbecco's modified Eagle's Medium (DMEM) with phenol red supplemented with 10% (v/v) Fetal Bovine Serum (FBS), 2 mM L-glutamine, 100 unitsmL⁻¹ penicillin and 100 µgmL⁻¹ streptomycin. This was named complete DMEM (cDMEM). The cells were passaged once a week (at 75-80% of confluence) at a density of 2.8 x 10⁴ cellcm⁻².

The day before the experiment, cells were seeded into a 96 well plate at a density of 10 x 10³ cells per well (100 µL). Prior to the treatments, cells were washed once with PBS. The MOFs were suspended in cDMEM by sonication at different concentrations, added to the cells and incubated – with 5 replicates for each variable (n = 5) – for 72 h at 37 °C with 5% CO₂. After 72 hours, the conditions were removed and the cells were washed once with phosphate buffered saline (PBS) to remove excess MOF, the media was replaced with 100 µL of fresh culture media containing 20 µL of MTS/phenazinemethosulfate (in a proportion 20:1) solution, and the plate was incubated for 1 h at 37 °C with 5% CO₂. Before reading the plates the plates at 490 nm by UV/vis spectrophotometry, the cell growth media was changed to a new plate to avoid false reading due to MOFs plate blockage.

The MTS assay for NaDCA is shown in Figure S28, and confirms that DCA has little effect on cell proliferation. A dose-responsive cytotoxicity is evident, but only at very high concentrations, with 40.6 ± 18.2% viability after incubation with 9 mgmL⁻¹ of NaDCA. This is in comparison with a maximum dose of 0.26 mgmL⁻¹ DCA delivered by the DCA@MOFs (26.4% w/w loading of DCA in DCA@Zr-L4_{small}, incubated at 1 mgmL⁻¹ MOF). After incubation with 0.5 mgmL⁻¹ NaDCA, the viability of MCF-7 cells is 99.9 ± 26.0%, and we have previously shown the empty MOFs to be non-toxic,^{S6} thus, any cytotoxicity comes from enhanced delivery of DCA into the MCF-7 cells by the MOF nanoparticles.

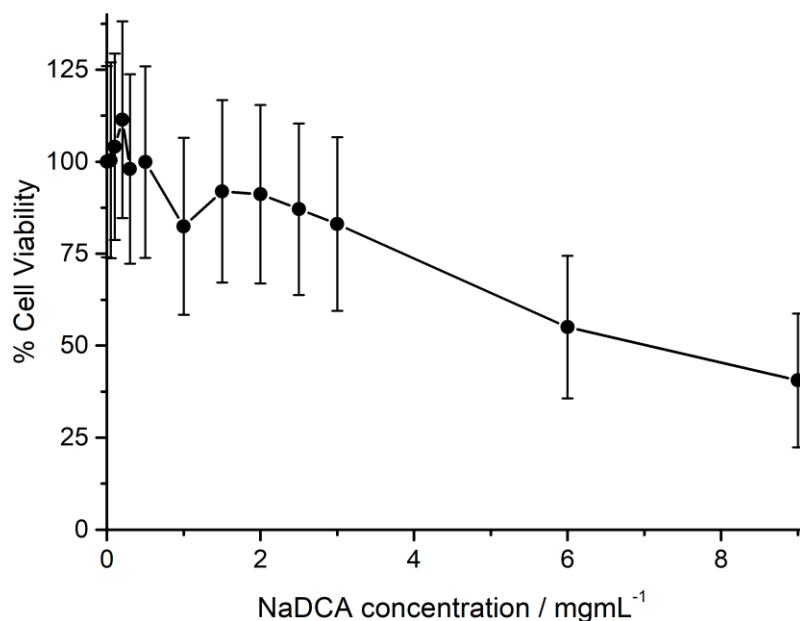


Figure S28. Viability, as measured by MTS proliferation assay, of MCF-7 cells when incubated with different concentrations of sodium dichloroacetate for 72 h.

Figure S29 shows the MCF-7 cell proliferation values when incubated with the larger DCA-loaded nanoparticles, plotted against MOF concentration. The analogous chart plotted against DCA concentration is shown in Figure 3a in the manuscript, and absolute values are collated in Table S7.

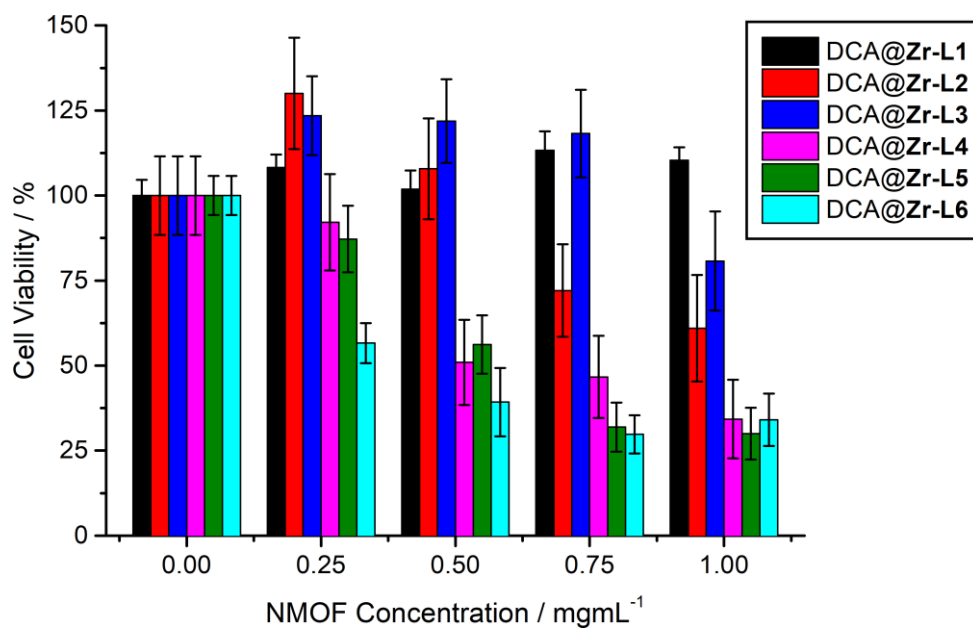


Figure S29. Viability, as measured by MTS proliferation assay, of MCF-7 cells when incubated with different concentrations of the larger DCA@MOF nanoparticles for 72 h.

Table S7. MCF-7 cell viabilities after incubation with different concentrations of the larger size DCA@MOFs for 72 h.

Conc / mgmL ⁻¹	DCA@ Zr-L1	DCA@ Zr-L2	DCA@ Zr-L3	DCA@ Zr-L4	DCA@ Zr-L5	DCA@ Zr-L6
0	100 ± 4.6	100 ± 11.5	100 ± 11.5	100 ± 11.5	100 ± 5.7	100 ± 5.7
0.25	108.3 ± 3.8	130.0 ± 16.4	123.5 ± 11.6	92.1 ± 14.5	87.2 ± 9.8	56.6 ± 5.9
0.5	101.9 ± 5.6	107.9 ± 14.8	121.8 ± 12.3	50.9 ± 12.9	56.2 ± 8.6	39.2 ± 10.1
0.75	113.3 ± 5.6	72.1 ± 13.6	118.2 ± 12.9	46.6 ± 12.1	31.9 ± 7.2	29.8 ± 5.6
1	110.7 ± 3.8	61.0 ± 15.7	80.8 ± 14.6	34.2 ± 11.5	30.0 ± 7.6	34.0 ± 7.7

Figure S30 shows a comparison of MCF-7 cell proliferation on incubation with the small and large terephthalate MOFs, plotted against MOF concentration. The analogous chart plotted against DCA concentration is given in Figure S31 (and partially in Figure 3b in the main text). Absolute values from Figure S30 are collated in Table S8.

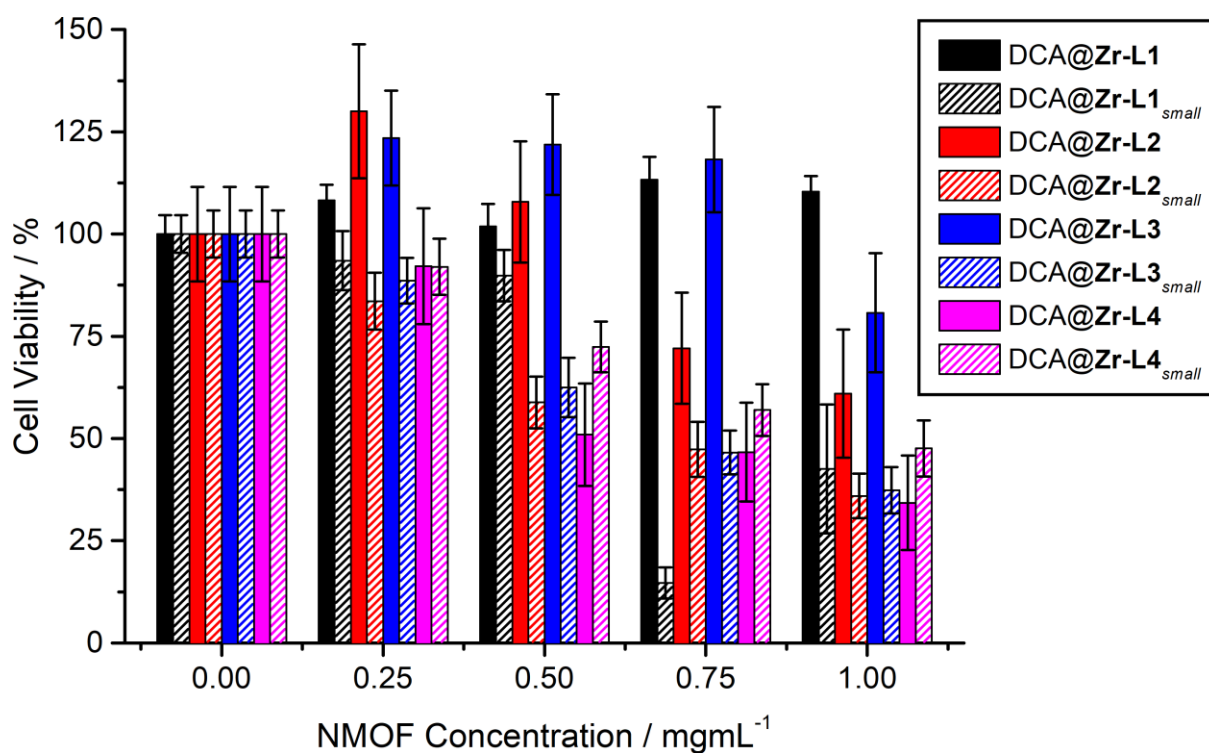


Figure S30. Comparison of the viability, as measured by MTS proliferation assay, of MCF-7 cells when incubated with different concentrations of the DCA-loaded terephthalate MOF nanoparticles of different sizes for 72 h.

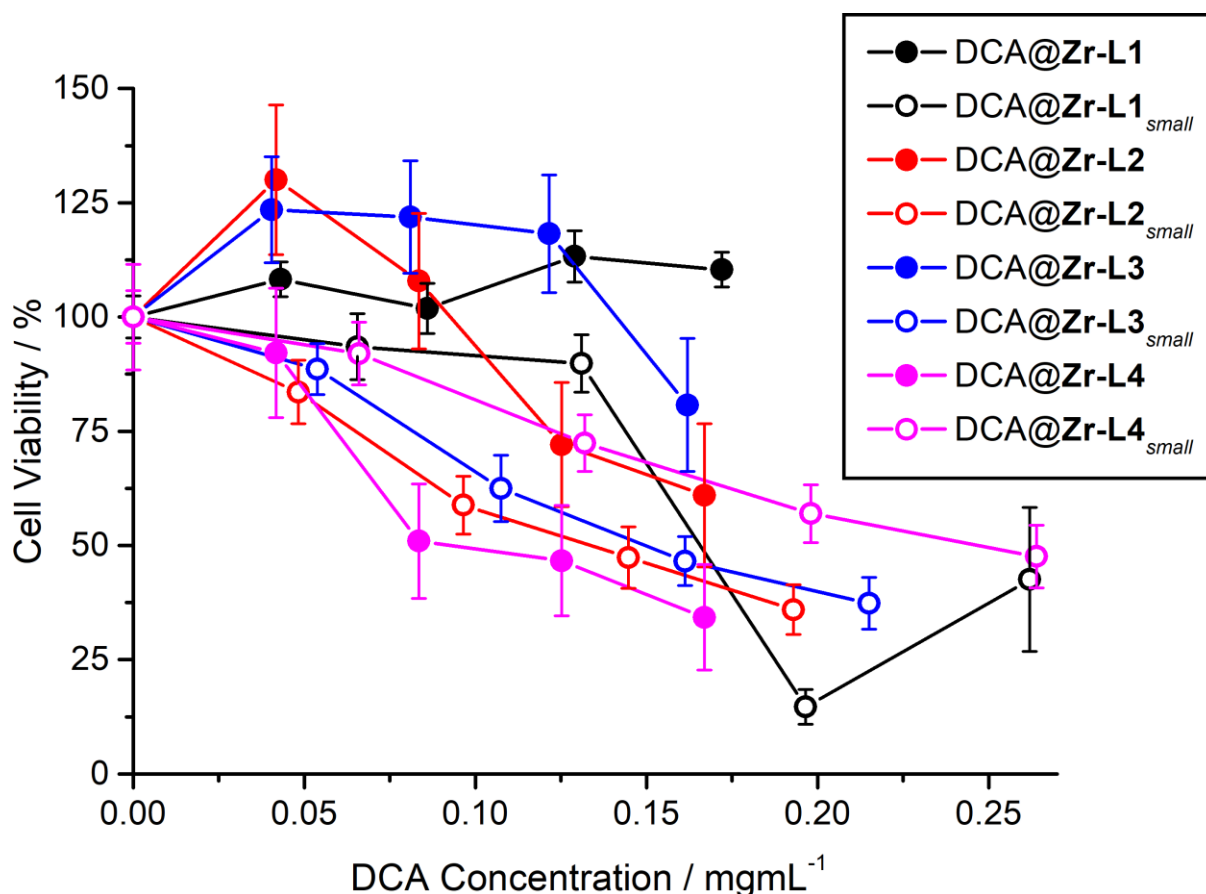


Figure S31. Comparison of the viability, as measured by MTS proliferation assay, of MCF-7 cells when incubated with different concentrations of the DCA-loaded terephthalate MOF nanoparticles of different sizes for 72 h, plotted against DCA concentration of the DDSs rather than MOF concentration.

Table S8. MCF-7 cell viabilities when incubated with different concentrations of the DCA-loaded Zr terephthalate MOFs of different sizes for 72 h.

Conc / mgmL ⁻¹	DCA@ Zr-L1 _{small}	DCA@ Zr-L2 _{small}	DCA@ Zr-L3 _{small}	DCA@ Zr-L4 _{small}	DCA@ Zr-L1	DCA@ Zr-L2	DCA@ Zr-L3	DCA@ Zr-L4
0	100 ± 4.6	100 ± 5.7	100 ± 5.7	100 ± 5.7	100 ± 4.6	100 ± 11.5	100 ± 11.5	100 ± 11.5
0.25	93.5 ± 7.2	83.6 ± 6.9	88.6 ± 5.6	92.0 ± 6.9	108.3 ± 3.8	130.0 ± 16.4	123.5 ± 11.6	92.1 ± 14.5
0.5	89.8 ± 6.3	58.8 ± 6.3	62.5 ± 7.3	72.4 ± 6.2	101.9 ± 5.6	107.9 ± 14.8	121.8 ± 12.3	50.9 ± 12.9
0.75	14.6 ± 3.8	47.3 ± 6.7	46.6 ± 5.4	57.0 ± 6.3	113.3 ± 5.6	72.1 ± 13.6	118.2 ± 12.9	46.6 ± 12.1
1	42.5 ± 15.7	36.0 ± 5.4	37.3 ± 5.7	47.6 ± 6.8	110.7 ± 3.8	61.0 ± 15.7	80.8 ± 14.6	34.2 ± 11.5

S6. 5-FU Loading

The known anticancer drug 5-fluorouracil (5-FU) was loaded into the DCA-loaded MOFs to examine the effect of dual drug delivery and the reports that DCA can enhance the therapeutic efficiency of 5-FU.^{S10, S11}

5-FU Loadings:

40 mg of the DCA@NMOF in question were sonicated during 15 minutes in a 5-FU solution (3 mgmL⁻¹ in MeOH), and then the dispersion was stirred during 3 hours at room temperature. The 5-FU@DCA@NMOFs were collected by centrifugation and washed with MeOH (x2) through dispersion centrifugation cycles to ensure no residual 5-FU was present on the surfaces of the particles. The resultant NMOFs were dried under vacuum at least 24 hours before analysis.

FT-IR and NMR spectroscopies were again attempted to determine the extent of 5-FU loading. ¹H NMR spectra of acid digested samples showed that DCA was still present after loading, but only very low intensity signals were observed for 5-FU, indicating low loading. Additionally, due to the very low content of 5-FU, its FT-IR vibration bands are masked by the MOF signals in the FT-IR spectra of the 5-FU@DCA@MOF samples. The characteristic vibration bands of DCA can still clearly be observed in the spectra (Figure S32).

Thermogravimetric analysis of the samples (Figure S33) is complicated by the fact that 5-FU and DCA thermally decompose in the same temperature region (250–375 °C). As such, it is not possible to quantify 5-FU loading using TGA.

To overcome this issue, a spectrophotometric protocol was developed to take advantage of the characteristic UV/Vis spectrum of 5-FU and allow determination of 5-FU loading values.

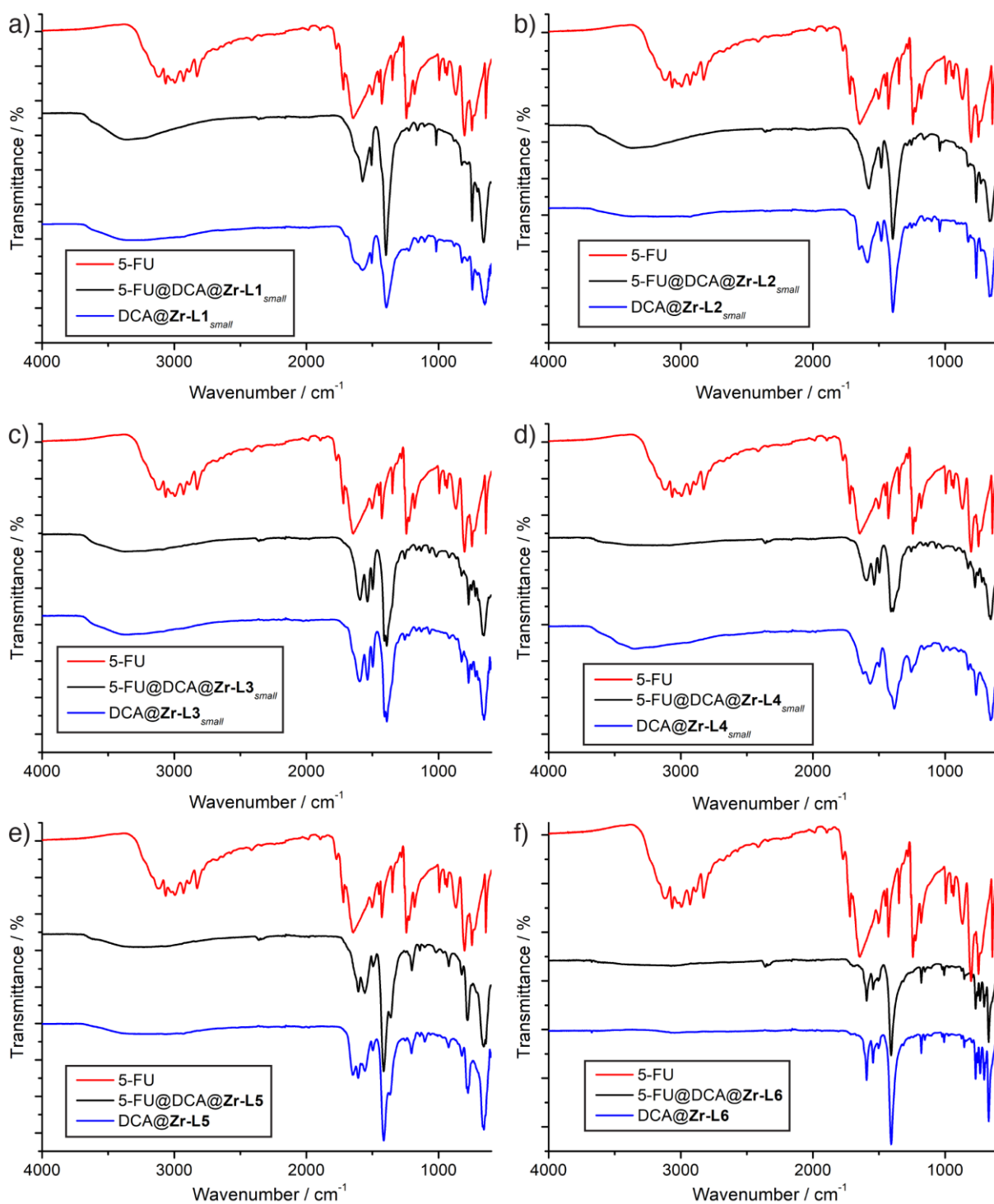


Figure S32. Comparison of FTIR spectra of DCA and 5-FU loaded MOFs compared to the DCA-loaded MOF and 5-FU for a) 5-FU@DCA@Zr-L₁_{small}, b) 5-FU@DCA@Zr-L₂_{small}, c) 5-FU@DCA@Zr-L₃_{small}, d) 5-FU@DCA@Zr-L₄_{small}, e) 5-FU@DCA@Zr-L₅, and f) 5-FU@DCA@Zr-L₆.

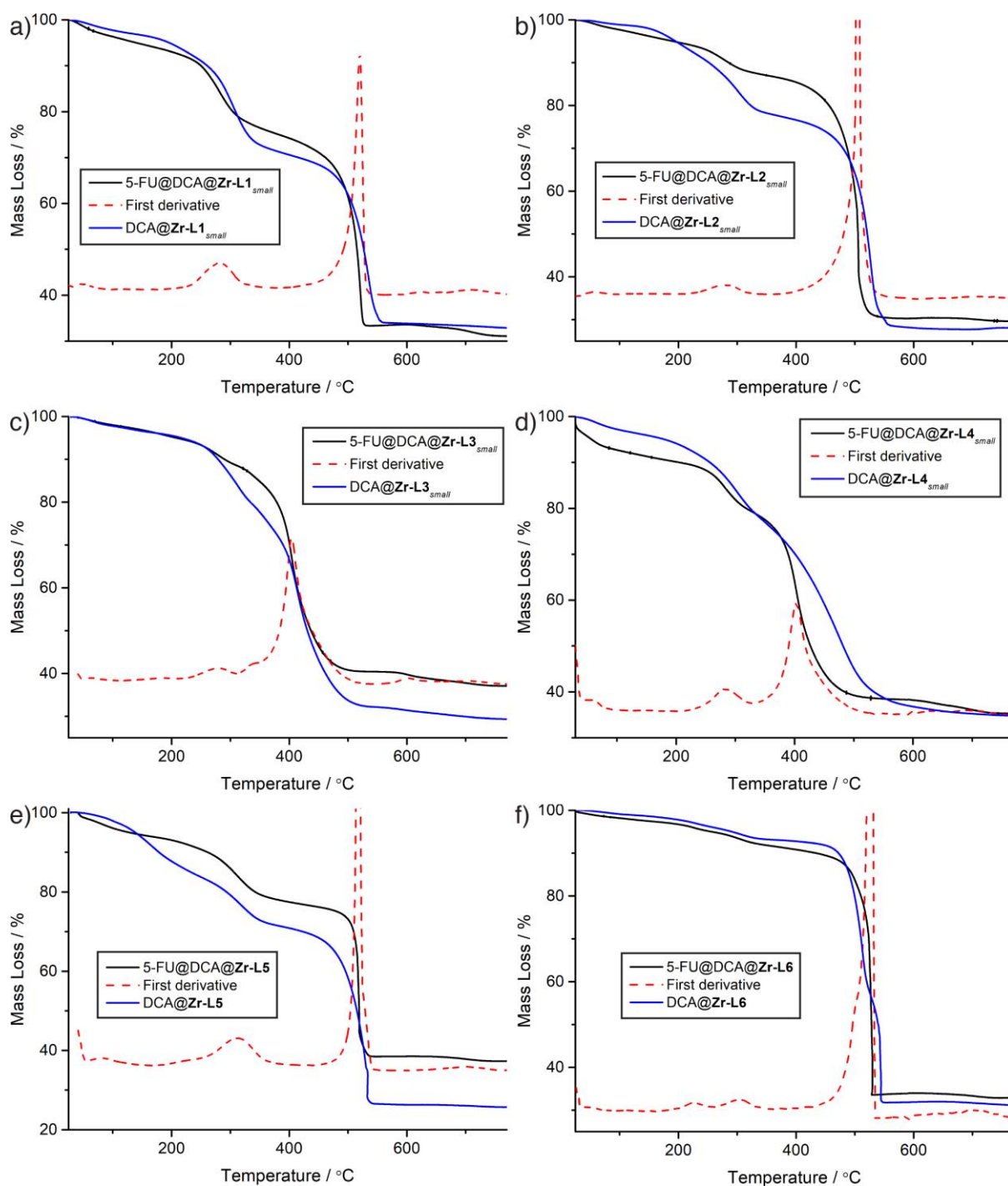


Figure S33. Comparison of TGA traces of the DCA and 5-FU loaded MOFs compared to the DCA-loaded analogues for a) 5-FU@DCA@Zr-L1_{small}, b) 5-FU@DCA@Zr-L2_{small}, c) 5-FU@DCA@Zr-L3_{small}, d) 5-FU@DCA@Zr-L4_{small}, e) 5-FU@DCA@Zr-L5, and f) 5-FU@DCA@Zr-L6.

5-FU Loading Determination by UV-Vis Spectroscopy:

Since the main UV-Vis absorbance band of 5-FU ($\lambda_{\max} = 266 \text{ nm}$) overlaps with the absorbance of L2 and L3 in particular, determination of 5-FU content through digestion of the samples in PBS is not possible. However, the MOFs are stable in methanol, showing minimal leakage and enabling 5-FU release and determination against a previously calculated calibration curve

Around 2.5 mg of samples were dispersed in 5 mL of MeOH and sonicated for 2 minutes in order to promote 5-FU release, followed by 30 minutes stirring at room temperature. The supernatant was collected by centrifugation, and a UV/Vis spectrum measured from $\lambda = 200\text{-}500 \text{ nm}$. The 5-FU content ($\lambda_{\max} = 266 \text{ nm}$) in weight percent was calculated against a previously calculated calibration curve (Figure S34). Additionally, absorbance measurements of the linkers in MeOH were performed, confirming minor or no linker leakage from the MOFs that did not affect 5-FU determination. UV/Vis spectra of 5-FU release are provided in Figure S35, and loading values are given in Table 1 in the main manuscript. The calculations were performed using the exact mass of each MOF added. The samples were dispersed again and the measurements were repeated 2 hours after to ensure that 5-FU release was completed.

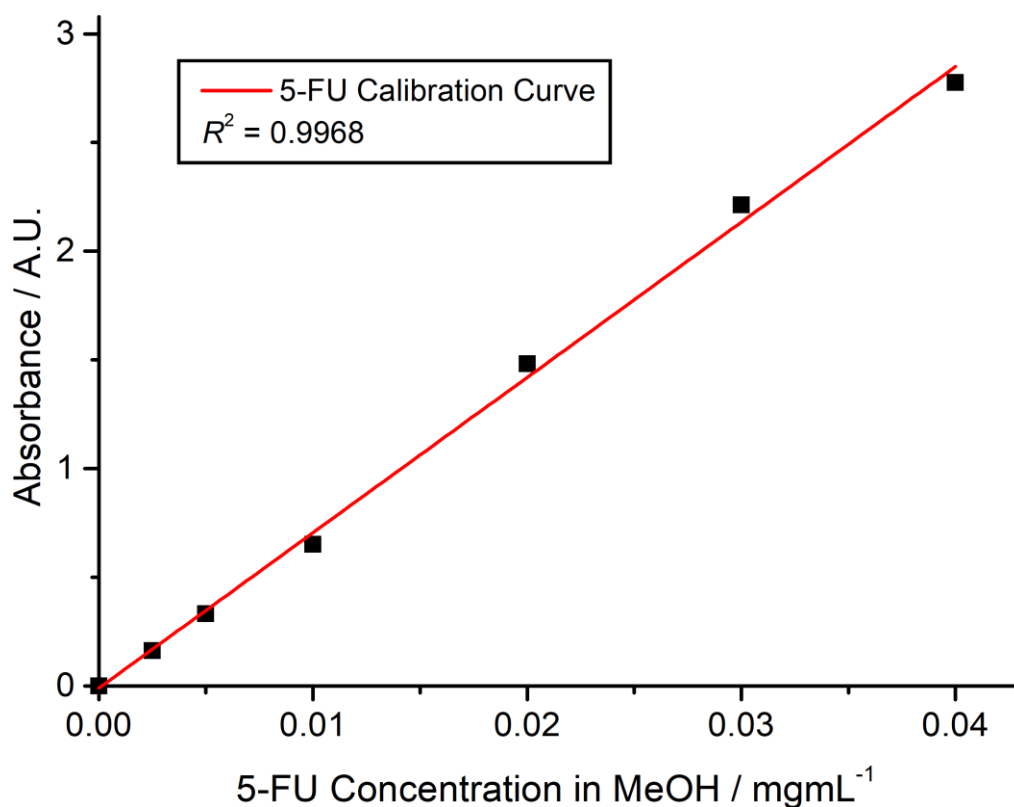


Figure S34. Calibration curve of 5-FU in methanol.

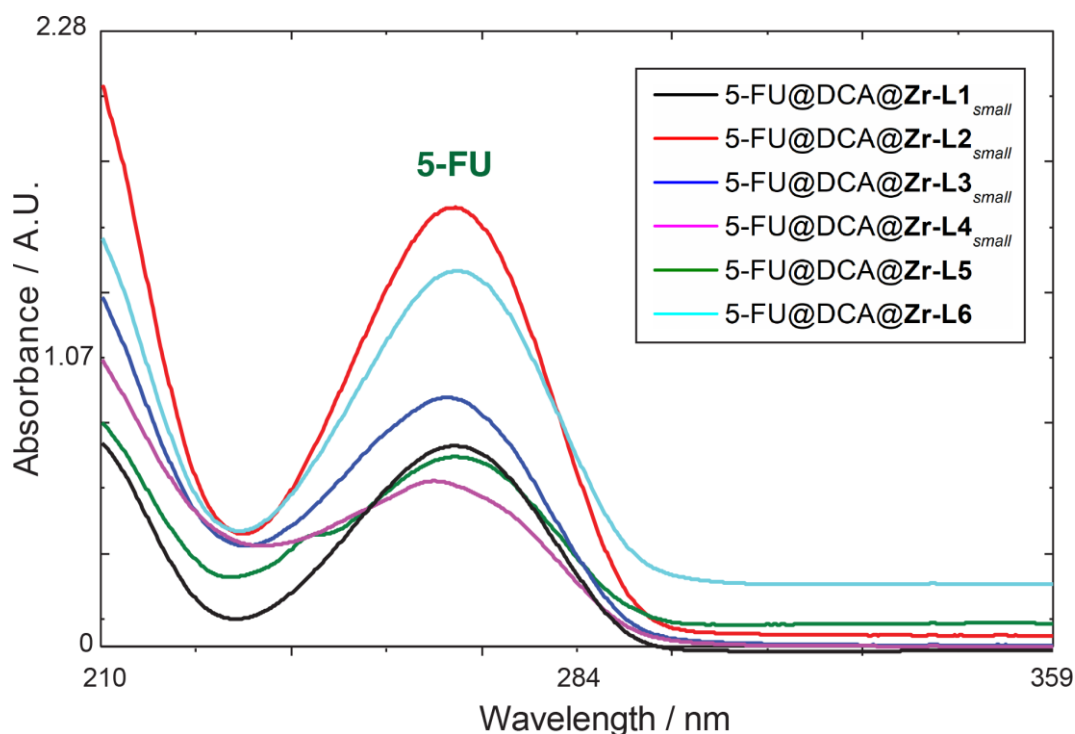


Figure S35. Release of 5-FU into methanol from the 5-FU@DCA@MOFs followed by UV/Vis spectroscopy to allow determination of 5-FU loading.

Knowing the loading of 5-FU in the MOFs, it is therefore possible to estimate the DCA loading using the TGA traces shown in Figure S33, if we assume that the mass loss in the temperature region (250–375 °C) corresponds to thermal decomposition of both DCA and 5-FU, and therefore deduct the 5-FU content, as determined by UV/Vis spectroscopy, from the total (Table S9). The terephthalate-based MOFs lose significant quantities of DCA during 5-FU loading, but still retain respectable, clinically relevant contents.

Table S9. Estimation of DCA loading in the 5-FU@DCA@NMOFs by a combination of TGA analysis and UV/Vis spectroscopy.

Sample	% 5-FU	% TGA	% DCA ^a
5-FU@DCA@Zr-L1 _{small}	1.9	24.1	22.3 (26.2)
5-FU@DCA@Zr-L2 _{small}	3.8	16.9	13.1 (19.3)
5-FU@DCA@Zr-L3 _{small}	4.3	13.0	8.7 (21.5)
5-FU@DCA@Zr-L4 _{small}	2.4	15.0	12.6 (26.4)
5-FU@DCA@Zr-L5	1.5	17.0	15.5 (14.1)
5-FU@DCA@Zr-L6	2.5	9.6	7.1 (6.6)

^aValues in brackets are DCA loadings determined for the samples prior to 5-FU loading for comparison.

S7. Therapeutic Efficiency of 5-FU@DCA@MOFs

5-FU acts as a thymidylate synthase (TS) inhibitor, and thus needs to reach the nucleus of cancer cells to be effective,^{S12} while DCA inhibits pyruvate kinase and hence acts in the mitochondria.^{S13-S15} As such, the efficacy of both drugs depends on localisation in the cytosol after uptake, and so successful delivery of both drugs into the cytosol of cancer cells by one DDS may result in enhancement of therapeutic activity.

The MTS cell viability assays for MCF-7 cells incubated with 5-FU@DCA@MOFs were performed following the same protocol as in Section S5 for the DCA@MOFs. Additionally, the MTS assay was carried out against free 5-FU to determine its therapeutic efficiency. The results are plotted in Figure 4 in the main text and the absolute values tabulated in Table S10.

Table S10. MCF-7 cell viabilities when incubated with different concentrations of free 5-FU for 72 h.

Free 5-FU / mgmL ⁻¹	Cell viability (%)
0	100.0 ± 14.0
0.005	96.1 ± 15.0
0.01	109.8 ± 15.0
0.0125	92.1 ± 14
0.015	50.9 ± 12.6
0.0175	46.6 ± 12.1
0.02	34.2 ± 11.5
0.025	8.2 ± 12.7
0.05	10.0 ± 13.0

Free 5-FU has significant cytotoxicity under these conditions, presumably after uptake into the MCF-7 cells by passive diffusion. The 5-FU loadings in the 5-FU@DCA@MOFs mean that individual MTS assay experiments under the same conditions and MOF concentrations as in the Section S5 will result in delivery of very low quantities of 5-FU (see Table S11). The 5-FU concentrations achieved by the 5-FU@DCA@MOFs dispersed in growth media are in the range of non-cytotoxic and cytotoxic free 5-FU concentrations, which allows determination of any enhancement in cytotoxicity compared to free 5-FU. The results are plotted in Figure 4 in the main text and the absolute values collated in Table S12.

Table S11. Individual concentrations of 5-FU delivered by each MOF at each concentration during the cell proliferation assays.

MOF conc / mgmL ⁻¹	5-FU@ DCA@ Zr-L1_{small}	5-FU@ DCA@ Zr-L2_{small}	5-FU@ DCA@ Zr-L3_{small}	5-FU@ DCA@ Zr-L4_{small}	5-FU@ DCA@ Zr-L5	5-FU@ DCA@ Zr-L6
0.25	0.00475	0.0095	0.01075	0.006	0.00375	0.00625
0.5	0.0095	0.019	0.0215	0.012	0.0075	0.0125
0.75	0.01425	0.0285	0.03225	0.018	0.01125	0.01875
1	0.019	0.038	0.043	0.024	0.015	0.025

Table S12. MCF-7 cell viabilities when incubated with different concentrations of the 5-FU@DCA@MOFs for 72 h.

MOF conc / mgmL ⁻¹	5-FU@ DCA@ Zr-L1_{small}	5-FU@ DCA@ Zr-L2_{small}	5-FU@ DCA@ Zr-L3_{small}	5-FU@ DCA@ Zr-L4_{small}	5-FU@ DCA@ Zr-L5	5-FU@ DCA@ Zr-L6
0	100 ± 4.6	100 ± 6.7	100 ± 6.7	100 ± 6.7	100 ± 6.7	100 ± 6.7
0.25	62.0 ± 13.5	77.3 ± 7.9	60.4 ± 8.6	85.1 ± 12.1	26.7 ± 6.6	4.0 ± 6.3
0.5	53.8 ± 8.0	55.6 ± 8.7	18.8 ± 6.7	33.1 ± 8.4	6.7 ± 6.3	3.7 ± 6.4
0.75	33.8 ± 8.4	40.1 ± 11.4	18.0 ± 7.3	6.2 ± 6.5	4.1 ± 6.3	5.0 ± 6.4
1	20.9 ± 7.3	21.2 ± 6.6	13.1 ± 6.7	2.4 ± 6.3	4.7 ± 6.5	5.4 ± 6.5

Control experiments were carried out to assess the enhancement in cytotoxicity when 5-FU and DCA are delivered in a bimodal fashion by the Zr MOFs. MTS assays on a new batch of MCF-7 cells were carried out in the presence of (i) free 5-FU, (ii) free 5-FU spiked with 0.1 mgmL⁻¹ NaDCA, and (iii) free 5-FU spiked with 0.2 mgmL⁻¹ NaDCA using the conditions described in Section S5. The addition of NaDCA was designed to mimic the concentrations of DCA delivered by the 5-FU@DCA@MOFs in the experiments described in Section S5; the results are shown in Figure S36 and tabulated in Table S13. The results are the same within experimental error, showing that no enhancement of 5-FU cytotoxicity occurs when administered with free DCA at these concentrations, which is presumably a consequence of the fact that DCA cannot efficiently cross the cell membrane without a suitable DDS. Literature reports of enhanced 5-FU cytotoxicity when administered alongside DCA require concentrations of DCA one or two orders of magnitude higher than those delivered by the MOFs,^{S10, S11} again demonstrating the potential of MOFs to transport DCA across the cell membrane.

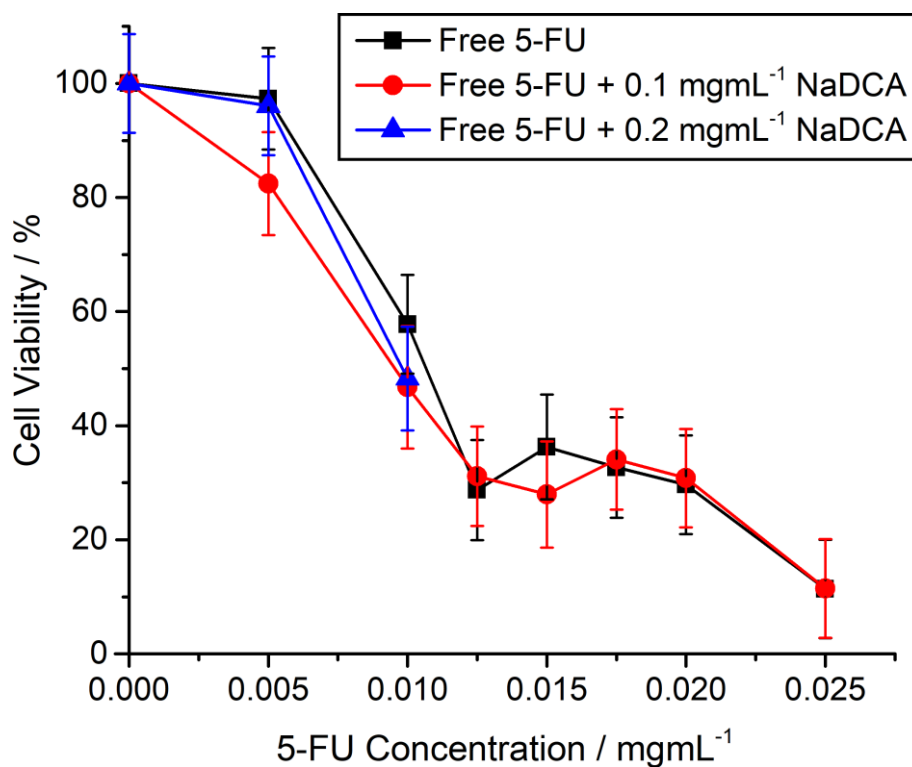


Figure S36. Comparison of the viability, as measured by MTS proliferation assay, of MCF-7 cells when incubated with different concentrations of 5-fluoruracil, spiked with different concentrations of NaDCA, for 72 h.

Table S13. MCF-7 cell viabilities when incubated with different concentrations of 5-fluoruracil, spiked with different concentrations of NaDCA, for 72 h.

5-FU conc / mgmL ⁻¹	Free 5-FU	+ NaDCA (0.1 mgmL ⁻¹)	+ NaDCA (0.2 mgmL ⁻¹)
0	100 ± 8.6	100 ± 8.6	100 ± 8.6
0.005	97.3 ± 8.9	82.5 ± 9.0	96.1 ± 8.7
0.01	57.8 ± 8.7	46.8 ± 10.7	48.3 ± 9.1
0.0125	28.7 ± 8.8	31.2 ± 8.7	
0.015	36.3 ± 9.2	27.9 ± 9.3	
0.0175	32.7 ± 8.8	34.1 ± 8.8	
0.02	29.7 ± 8.7	30.8 ± 8.6	
0.025	11.4 ± 8.6	11.5 ± 8.6	

Slightly different cytotoxicities of free 5-FU towards MCF-7 cells were observed at low 5-FU concentrations when compared to the data previously collected in Section S5, presumably as a consequence of these additional MTS assays being carried out on a completely new

batch of MCF-7 cells. When the average cell proliferation values from these two independent MTS assays are plotted against the cell proliferation values previously determined for the 5-FU@DCA@MOFs (Figure S37), the trends described in the manuscript and in Section S5 are still evident, and the conclusions and hypotheses made do not change. These experiments show that, when comparing absolute values from MTS cell proliferation assays, it is important to collect data from assays run concurrently on the same batch of cells to ensure experimental error is reduced. The data presented in Figure 4b in the manuscript come from assays carried out on the same batch of cells at the same time, which should give a better comparison.

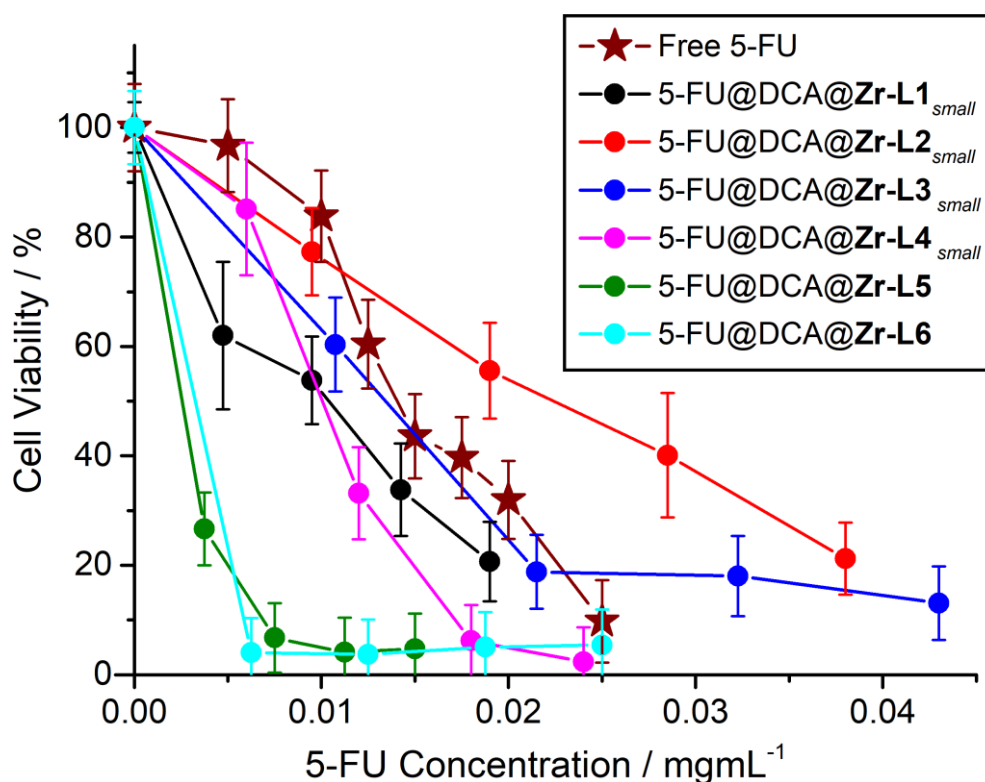


Figure S37. Comparison of MTS cell proliferation assays of 5-FU@DCA@MOFs plotted against 5-FU concentration compared to a value for free 5-FU that is the average of two separate sets of assays carried out at different times on different batches of MCF-7, in comparison with Figure 4b in the main manuscript.

S8. References

- S1. B. Bueken, N. Van Velthoven, T. Willhammar, T. Stassin, I. Stassen, D. A. Keen, G. V. Baron, J. F. M. Denayer, R. Ameloot, S. Bals, D. De Vos and T. D. Bennett, *Chem. Sci.*, 2017, **8**, 39393948.
- S2. G. C. Shearer, S. Chavan, S. Bordiga, S. Svelle, U. Olsbye and K. P. Lillerud, *Chem. Mater.*, 2016, **28**, 3749–3761.
- S3. M. J. Cliffe, W. Wan, X. Zou, P. A. Chater, A. K. Kleppe, M. G. Tucker, H. Wilhelm, N. P. Funnell, F. X. Coudert and A. L. Goodwin, *Nat. Commun.*, 2014, **5**, 4176.
- S4. F. Rouquerol, J. Rouquerol and K. Sing, in *Adsorption by Powders and Porous Solids*, Academic Press, London, 1999, 191–217.
- S5. D. R. Lide, *CRC Press, Taylor & Francis, Boca Raton*, 2005, 3–150.
- S6. C. Orellana-Tavra, R. J. Marshall, E. F. Baxter, I. Abánades Lázaro, A. Tao, A. K. Cheetham, R. S. Forgan and D. Fairen-Jimenez, *J. Mater. Chem. B*, 2016, **4**, 7697-7707.
- S7. J. H. Cavka, S. Jakobsen, U. Olsbye, N. Guillou, C. Lamberti, S. Bordiga and K. P. Lillerud, *J. Am. Chem. Soc.*, 2008, **130**, 13850–13851.
- S8. C. Orellana-Tavra, S. Haddad, R. J. Marshall, I. Abánades Lázaro, G. Boix, I. Imaz, D. MasPOCH, R. S. Forgan and D. Fairen-Jimenez, *ACS Appl. Mater. Interfaces*, 2017, **9**, 35516–35525.
- S9. E. Bellido, T. Hidalgo, M. V. Lozano, M. Guillevic, R. Simón-Vázquez, M. J. Santander-Ortega, Á. González-Fernández, C. Serre, M. J. Alonso and P. Horcajada, *Adv. Healthc. Mater.*, 2015, **4**, 1246–1257.
- S10. Y. Xuan, H. Hur, I.-H. Ham, J. Yun, J.-Y. Lee, W. Shim, Y. B. Kim, G. Lee, S.-U. Han and Y. K. Cho, *Exp. Cell Res.*, 2014, **321**, 219–230.
- S11. J. Tong, G. Xie, J. He, J. Li, F. Pan and H. Liang, *J. Biomed. Biotechnol.* 2011, 740564.
- S12. J. L. Grem, *Semin. Rad. Oncol.*, 1997, **7**, 249–259.
- S13. E. D. Michelakis, L. Webster and J. R. Mackey, *Br. J. Cancer*, 2008, **99**, 989–994.
- S14. E. D. Michelakis, G. Sutendra, P. Dromparis, L. Webster, A. Haromy, E. Niven, C. Maguire, T. L. Gammer, J. R. Mackey, D. Fulton, B. Abdulkarim, M. S. McMurtry and K. C. Petruk, *Sci. Transl. Med.*, 2010, **2**, 31ra34.
- S15. D. Heshe, S. Hoogstraat, C. Brauckmann, U. Karst, J. Boos and C. Lanvers-Kaminsky, *Cancer Chemother. Pharmacol.*, 2011, **67**, 647–655.